EPFL

ALFRED-WEGENER-INSTITUT
HELMHOLTZ-ZENTRUM FÜR POLAR-
UND MEERESFORSCHUNG

MASTER THESIS

Using a towed undulating platform to measure ocean velocities and to estimate turbulent dissipation rates

Laura MATHIEU

Advisor : Dr. Wilken-Jon VON APPEN
Physical Oceanography, AWI
Supervisor : Prof. Alfred Johny WÜEST
APHYS, EPFL

July 18, 2019

Abstract

The need for characterizing turbulence in the ocean recently led to new techniques, among which is the use of acoustic Doppler current profilers (ADCP) on various stationary and moving platforms. This study aims to estimate the dissipation of turbulent kinetic energy, ε, and the advective oceanic velocities from two 1.2-MHz single ping mode ADCPs mounted on a remotely operated towed vehicle (ROTV). The data consist of an equatorial transect of the Atlantic Ocean on which the ROTV was undulating between the surface and 300 meters depth. ε is then estimated from the second and third order structure functions. This work outlines the development and the results of the application of this method on the available dataset. The conclusion is that for this data set, the signal to noise ratio is too low. We recommend acquiring at least an order of magnitude more individual raw pings. This would more likely let the statistics coverage to a reliable estimate of ε. Additionally, prior knowledge of the Ozmidov scale, i.e. the size of the largest overturning eddies, is helping to ensure that roughly ten bins are within the inertial subrange. This approach enables continuous measurements of profiles for a whole transect, as well as measurements close to the surface by operating the ROTV outside the vessel-induced turbulence zone. This new technique has the advantage to broaden the measurement range of high-frequency ADCP measurements by the undulation of the vehicle.

Coverpage picture: TRIAXUS and its upward looking ADCP, 21 November 2018.

Résumé

La nécessité de caractériser la turbulence dans les océans a récemment conduit à l'élaboration de nouvelles techniques, parmi lesquelles l'utilisation de courantomètres acoustiques Doppler (en anglais, ADCP), installés sur diverses plateformes fixes et mobiles. Cette étude vise à estimer la dissipation de l'énergie cinétique turbulente, ε, en utilisant deux 1.2-MHz ADCP fonctionnant en mode "single-ping" et fixés sur un véhicule tracté téléguidé (en anglais, ROTV). Les données consistent en un transect équatorial de l'océan Atlantique le long duquel le véhicule ondulait entre la surface et une profondeur de 300 mètres. ε est ensuite estimé en utilisant la "structure-function" de deuxième et troisième ordre. Ce travail présente le développement et les résultats de l'application de cette méthode. Il en ressort que, pour l'ensemble de données de l'équateur, le rapport signal sur bruit est trop faible. Il est ainsi recommandé d'acquérir au moins un ordre de grandeur de données brutes supplémentaire. Cela permettrait une estimation de ε fiable, basée sur une plus grande couverture statistique. De plus, une connaissance préalable de l'échelle d'Ozmidov, i.e. la taille des plus grands tourbillons, est utile pour garantir qu'au moins une dizaine de "bins" se situent en dessous de cette grandeur. Cette approche permet de mesurer continuellement des profils le long d'un transect sans travail laborieux. De plus, elle permet également des mesures proche de la surface en utilisant le véhicule hors de la zone de turbulence induite par le navire. Cette nouvelle technique présente l'avantage d'élargir la plage de mesure des mesures d'un ADCP à haute fréquence via l'ondulation du ROTV.

Mots-clefs: turbulence, dissipation, courantomètres acoustiques Doppler (ADCP), plateforme tractée, ondulant, profil de vitesses

Nomenclature

Acronyms

ADCP	Acoustic Doppler Current Profiler
AUV	Autonomous Underwater Vehicle
AWI	Alfred Wegener Institute, Helmholtz Centre for Polar and Marine Research
CTD	Conductivity-Temperature-Depth probe
EPFL	École Polytechnique Fédérale de Lausanne
EUC	Equatorial Undercurrent
GAPS	iXblue Gaps system
GPS	Global Positioning System
IGRF	International Geomagnetic Reference Field
ITCZ	Intertropical Convergence Zone
PS113	Expedition of the research vessel POLARSTERN across the Atlantic Ocean in 2018
R/V	Research Vessel
ROTV	Remotely Operated Towed Vehicle
SST	Sea Surface Temperature
TKE	Turbulent Kinetic Energy
topAWI	Towed ocean profiler of the AWI
UTC	Coordinated Universal Time
VMADCP	Vessel-Mounted ADCP

Variables

η	Kolmogorov microscale
ν	Kinematic viscosity
ε	Dissipation of turbulent kinetic energy
D_n	n-th order structure function
L_o	Ozmidov scale
N	Buoyancy frequency, also called Brunt–Väisälä frequency

Table of contents

1 Introduction

1.1 Turbulent kinetic energy and its dissipation

The turbulent kinetic energy (TKE) and associated mixing play an essential role for vertical transport of momentum, heat and material in all stratified waters, such as the ocean. By making nutrients and light accessible for the phytoplankton, it may determine the primary production rate. The latter is an important contributor to removal of CO_2 from the atmosphere and it also determines the yield of fisheries.

TKE is the mean kinetic energy per volume contained in the eddies of a flow and is defined as:

$$TKE = \frac{1}{2}\rho \overline{(u'^2 + v'^2 + w'^2)} \,, \tag{1}$$

where ρ is the density, u', v' and w' are the fluctuation terms resulting from the Reynolds decomposition of all velocity components and the overbar denotes the mean.

Because it is hardly possible to measure TKE directly, its dissipation, ε, is often used as a representative parameter. In the turbulent kinetic energy balance equation, ε represents loss of TKE. It is defined as follows:

$$\varepsilon = \frac{1}{2}\nu \langle s_{ij} s_{ij} \rangle \,, \tag{2}$$

where ν is the kinematic viscosity, the $\langle\ \rangle$ operator is defined as the scalar product, and the strain rate tensor s_{ij} is calculated as follows:

$$s_{ij} = \left(\frac{\partial u_i}{\partial x_j} + \frac{\partial u_j}{\partial x_i} \right) \,. \tag{3}$$

Einstein notation ij implies that the product takes places over all three spatial dimensions and summed up over double occuring indices. In the ocean, values of ε range from 10^{-11} to 10^{-1} [W/kg], which is equal to [m^2/s^3] in SI units (Thorpe, 2005). A high value of TKE dissipation rate results from a large energy input, such as through shear friction and instabilities or external forcing, such as topography. In the literature, ε is also sometimes expressed in [W/m^3]. As the density of seawater is roughly 1025 kg/m^3, we use the following conversion: 10^3 [W/m^3] ≈ 1 [W/kg].

The turbulent regime usually spreads over many scales, between the largest ones where the energy is accumulated (Ozmidov scale L_o), and the smallest ones at which viscous dissipation occurs (Kolmogorov scale η). Between these two scales is the so-called inertial subrange, in which the energy transfers from big towards small scales. This process is known as energy cascade (Ozmidov, 1965). The Kolmogorov scales and Ozmidov scales are defined as follows:

$$\eta = \left(\frac{\nu^3}{\varepsilon} \right)^{\frac{1}{4}} \,. \tag{4}$$

$$L_o = \sqrt{\frac{\varepsilon}{N^3}} \,, \tag{5}$$

where ν is the kinematic viscosity and N is the buoyancy frequency.

There are different ways to estimate the dissipation rate ε. Direct measurements can be done through a shear-probe, usually mounted on microstructure profilers. A considerable part of the knowledge we possess about the TKE dissipation was acquired by means of such instruments (Wiles et al., 2006). However, shear probes have the disadvantage of requiring a lot of ship time for the measurements and to have a cumbersome data treatment (Greene et al., 2015). Hence, other indirect approaches were developed. The main ones are the Thorpe resorting, the structure function method, and the large-eddy method. While Thorpe resorting is done on Conductivity-Temperature-Depth (CTD) measurements, the last two methods use acoustic Doppler current profilers (ADCPs) data.

The large-eddy technique is based on the work of Gargett (1999). An analysis of scales permits to retrieve ε from the velocity and the length of the large eddies. However, this method requires fitting a scaling parameter by using other TKE dissipation profiles, for example with the help of a shear-probe. The structure function approach relies on the work of Kolmogorov (1941). Its main result is that, within the inertial subrange of the energy cascade, there is a defined relationship between ε and both the second and third order structure functions (D_2 and D_3). The details of the structure function method will be explained in Section 3.3.

In their study, Wiles et al. (2006) first proposed to use the structure function method (in this case D_2) to determine ε from a bed-mounted ADCP, which they found to be in good agreement with the values measured with freefall profilers. A few years later, Lucas et al. (2014) also successfully estimated the turbulent dissipation with the structure function method, using this time a tethered buoy on which an ADCP was mounted.

Recently, Horwitz and Hay (2017) used a horizontally looking ADCP attached on a subsurface buoy and applied both a second and a third order structure function method to estimate ε. They pointed out that time averaging of $5 \cdot 10^3$ to $1 \cdot 10^5$ individual measurements was not always enough to achieve a robust statistical estimate (mean) of ε. This was shown by positive values for the 3$^{\text{rd}}$ order structure function (which by definition, see Equation 12 below, should always be negative) for insufficiently time-averaged estimates. It should be noted that the studies of Wiles et al. (2006) and Horwitz and Hay (2017) were in shallow fast flowing tidal channels with correspondingly large $\varepsilon >$ 10^{-5} [W/kg].

Pan and Jay (2008) presented a method to retrieve east- and northward velocities from an ADCP mounted on a towed undulating platform (TRIAXUS) by using an ADCP mounted in the hull of a research vessel (VMADCP) as an external reference.

In this thesis, we use the structure function method to estimate TKE from a towed undulating platform, alongside with the calculation of velocity profiles. The method is tested on data from the Equatorial Atlantic, which is introduced next.

1.2   Study site: the Equatorial Atlantic

One of the most remarkable features at the equator is the Equatorial Undercurrent (EUC), also known as the Cromwell current. The current is made possible by the pressure gradient resulting from the trade winds and their positioning at the equator, including the absence of the Coriolis force.

From a zonal point of view, the trade winds blow from east to west, which pushes water in the upper ocean westwards. As these winds are not compensated with the equatorial Counter-currents, which occur around 8° north and south, the sea level at the equator is higher at the western end of the basin, i.e. at the Brazilian coast in case of the Atlantic. From a meridional point of view, there is an asymmetry in the location of the calms which is found north of the equator, at the so-called Intertropical Convergence Zone (ITCZ). This results in a divergence zone at the equator, with a convergence zone north of the equator (Dietrich et al., 1975). This transverse circulation allows then space for the EUC to flow eastward at the equator, as shown in Figure 1. Because the Coriolis force

vanishes at the equator and is very weak within 1-2° of latitude from the equator, down-pressure gradient flows – which in other parts of the ocean are impossible to be sustained for time scales beyond a few hours – can occur in the vicinity of the equator.
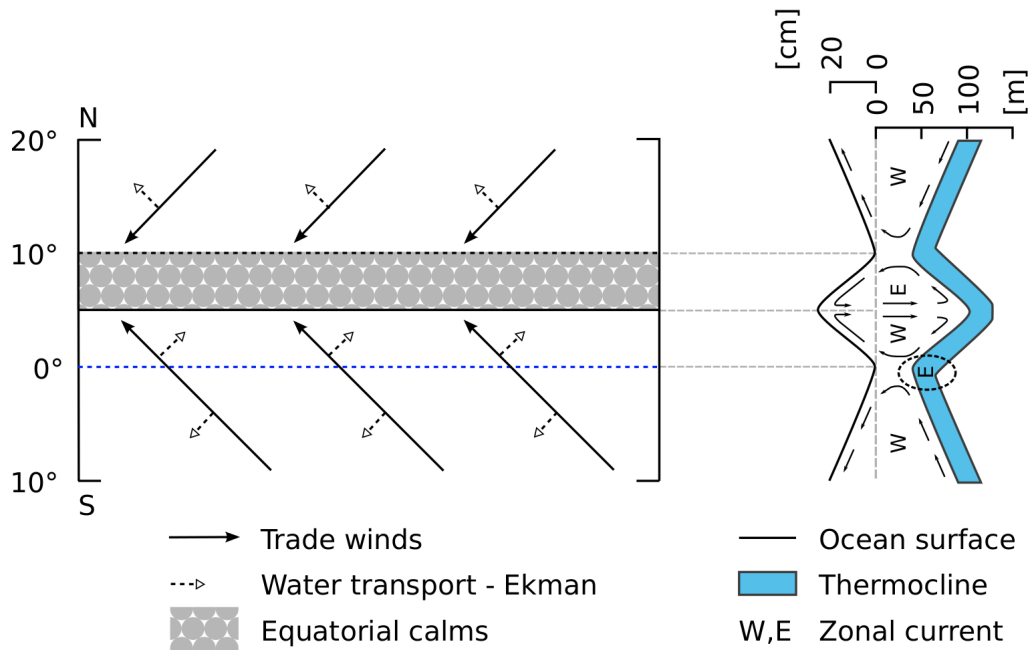

Figure 1: Schematics of the equatorial dynamics at the equator, adapted from Dietrich et al. (1975). On the left is a top-view with the trade winds and associated Ekman transport. Ekman transport is the net transport of water due to the wind, 90° to the right of the wind in the northern hemisphere and 90° to the left in the southern hemisphere. On the right is a meridional sectional view with transverse flows. East- and westwards currents are respectively out of and into the page.

The EUC in the Pacific flows eastwards with velocities exceeding 1 m/s. It transports between 20 and 50 Sverdrup (Sv, with 1 Sv = 10^6 m^3/s) and extends from approximately 30 m down to 200 m depth (Boyd, 2018). Its core coincides with the thermocline location (Knauss, 1960). As another comparison point, Butt and Lindstrom (1994) found values of 26.2 Sv for 153°E and 16.6 Sv for 149°E. Furthermore, based on a general circulation model, Blanke and Raynaud (1997) calculated the evolution of the EUC transport in terms of longitude (Figure 2), which shows the transport decreasing towards the east.
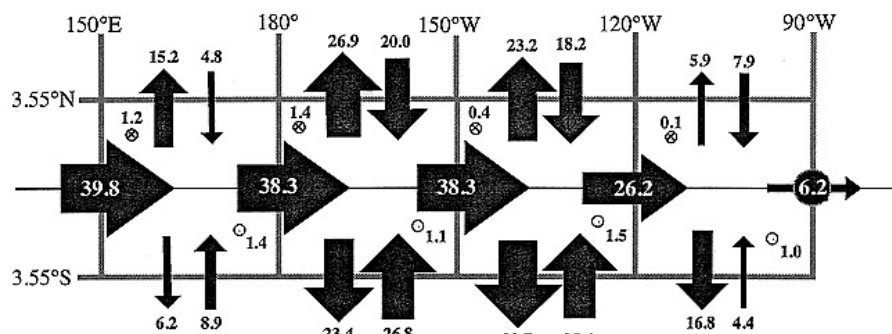

Figure 2: Mean annual mass exchanges in Sv at the equatorial Pacific, from 0 to 495 m depth. The horizontal arrows depict the EUC transport, whereas the vertical arrows refer to the meridional mass transport, and the circles represent vertical fluxes to (cross) and out (point) the 495 m depth layer (Blanke and Raynaud, 1997).

In the case of the Atlantic, the EUC flows with velocities of 0.8 to 1 m/s, and the core of the EUC is found to vary from ∼30 to 100 m with the shallower values located at the eastern boundary (Talley et al., 2011). In both oceans, due to the wind-driven westward flow at the ocean surface, the EUC is characterised by high shear at its top, leading to large turbulence. Therefore, a thin mixed layer is expected in this area, as well as a sharp thermocline.

Schott et al. (2003) found a total eastward transport of 20.9 Sv for the 35°W section of the EUC, with a major contribution of the surface layer above the 24.5 kg/m^3 isopycnal (line of constant potential density). They also remark on the shift of the ITCZ from ∼0° to 10°N with the higher ITCZ latitude reached during the boreal spring. Due to the ITCZ shift, the EUC is sometimes overlayed by an eastward current.

Henry (2018) argues that the complexity of equatorial dynamics leads to several knowledge gaps encountered in equatorial models. A most prevalent phenomenon is upwelling, which can be observed through enhanced biological activity at the surface. The productivity increases as nutrients are imported from below. In this rather turbulent context, the dissipation is expected to be significant.

As a matter of fact, Crawford and Osborn (1980) found typical values of $3 \cdot 10^{-7}$ W/kg for ε above the core of the EUC in the Atlantic, i.e. in their case between 70 and 40 m depth. In turn, Peters et al. (1988) indicate a value of 10^{-7} W/kg for the mean turbulent dissipation rate above the EUC core in the Pacific. Thorpe (2005) also emphasises that the latter is subject to fluctuations up to 2 orders of magnitude. This variation is due to the nocturnal convection. When the stratifying action of short wave solar radiation is removed, convection occurs and turbulence increases. More recently, Hummels et al. (2013) found values between $1\text{-}10 \cdot 10^{-7}$ W/kg above the EUC at a longitude of 10°W. Their distribution is shown in Figure 3. One can see that the dissipation rate varies by about 3 orders of magnitude at the equator, with higher values found above the EUC, which core was found at 50 m depth. All the estimates of ε found in the literature are summarized in Table 1.
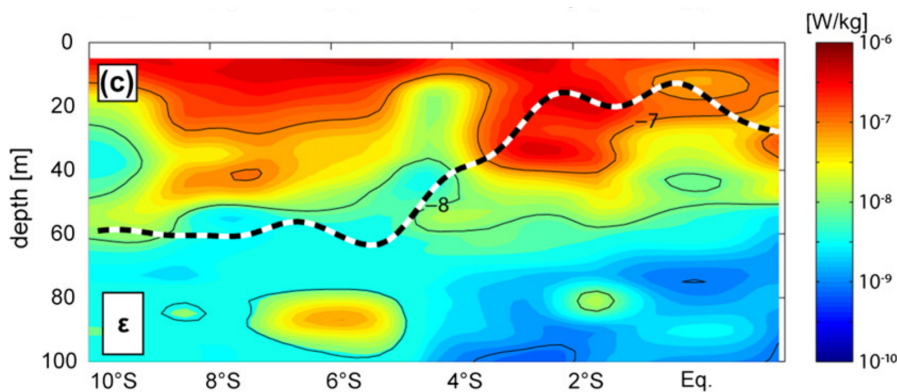

Figure 3: Estimates of TKE dissipation in [W/kg] for a transect at longitude 10°W from Hummels et al. (2013). Data was acquired with more than 780 microstructure profiles in June 2006. The EUC core was found at a depth of 50 m.

Table 1: Estimates for TKE dissipation rate above the core of the EUC from a literature review.

Paper	ε [W/kg]	Region
Crawford and Osborn (1980)	$3 \cdot 10^{-7}$	Atlantic, 28-32°W
Hummels et al. (2013)	$1 - 10 \cdot 10^{-7}$	Atlantic, 10°W
Peters et al. (1988)	$\approx 10^{-7}$	Pacific, 140°W

Also noteworthy is that two seasons can be distinguished in the Equatorial Atlantic Ocean (Voituriez and Herbland, 1979). A warm one from October to June and a cold between July and September, with the dissipation values most likely different between the two.

In the scope of this work, the EUC is not only a major component of the equatorial dynamics but also a current, whose well-known features ease the assessment of the measurements and the method development below.

1.3   Objectives of this thesis

One of the major issues in oceanography is the sparsity of the available data. The lack of comprehensive datasets is even more pronounced for turbulence estimates. Therefore time- and cost-effective measurement strategies are looked for. In this context, a towed undulating vehicle allows the completion of various measurements within much less ship time. In the present study, data from a towed undulating platform are analysed to assess if turbulence can be estimated from an ADCP. In addition, velocity profiles are calculated.

For this purpose, this thesis next introduces the data acquired during the PS113 cruise and points out the main critical points of this dataset. Then, the processing steps to get coherent velocity profiles and the structure function method applied to estimate turbulence are presented. Finally, after a discussion of the results, some recommendations are made for the future use of the platform for data acquisition.

2 Data

This section aims to present in detail what kind of information is available, how it was acquired and saved. The issues related to the operation of the instruments are raised here but will be tackled in Section 3.1.

The data used in this study was taken on the cruise of the research vessel (R/V) POLARSTERN PS113 across the Atlantic ocean, from Punta Arenas, Chile, to Bremerhaven, Germany. The whole expedition took place between 08.05.2018 and 11.06.2018. The complete ship track can be found in the appendix, Figure A1, and details of the cruise are specified in the cruise report (Strass, 2018b). This study will focus on the equatorial deployment of the topAWI platform, described hereafter.

2.1 Setup

TRIAXUS

The platform used for the measurements is a remotely operated towed vehicle (ROTV), the TRIAXUS from MacArtney Underwater Technology (Figure 4). Its flaps allow the cuboid vessel lateral and vertical displacements. The tether provides power and optical data transmission which means that the system can be controlled in real time from the vessel. A PC adjusts the desired trajectory of the platform in the water using onboard sensors for correction. The TRIAXUS enables undulations between the surface and a depth of 350 m, with a possible cross-track displacement of roughly 80 m on both sides behind the ship. The TRIAXUS can be operated with a towing speed between 2 to 10 knots (i.e. roughly 1 to 5 m/s) and a vertical speed up to 1 m/s. The main advantage of this system is that it allows to simultaneously measure many physical, chemical and biological properties in a volume of the ocean large enough to contain oceanographic (e.g. mesoscale) gradients within a time short enough that the ocean properties have not changed significantly before completion of the measurements.

topAWI

The TRIAXUS fiber optic connection, which can be seen in Figure A2, allows for other sensors to be attached. ADCP and CTD, among other probes, were mounted on TRIAXUS to form the new measuring system: the towed ocean profiler of AWI (topAWI). Raw velocity data is acquired with two Workhorse 1.2-MHz ADCPs from TELEDYNE RD Instruments, operated in single ping mode. In the following, we will also refer to the upward looking ADCP as ADCP1 and to the downward looking ADCP as ADCP2. Pressure, temperature, and conductivity are measured by a Sea-Bird 911+ CTD, with dual temperature and conductivity probes, and one pressure sensor. Another pressure probe is the one of the ROTV itself, mainly for steering purposes. Note that the ADCPs do not have pressure sensors. Finally, an iXblue Gaps system (GAPS) is also mounted on the platform. It can determine the position of the ROTV inside the water to better than $\pm$ 10 m. However, since it only works at speeds up to 6 knots, the GAPS was not functional on the transect exploited in the present study. The setup can be seen in Figure 4.

The topAWI was also optimised for undulations up to a theoretical threshold of 450 m depth, but for this particular cruise and configuration, pressure rating of the buoyancy foam limited operation to 350 m depth (Strass, 2018b).
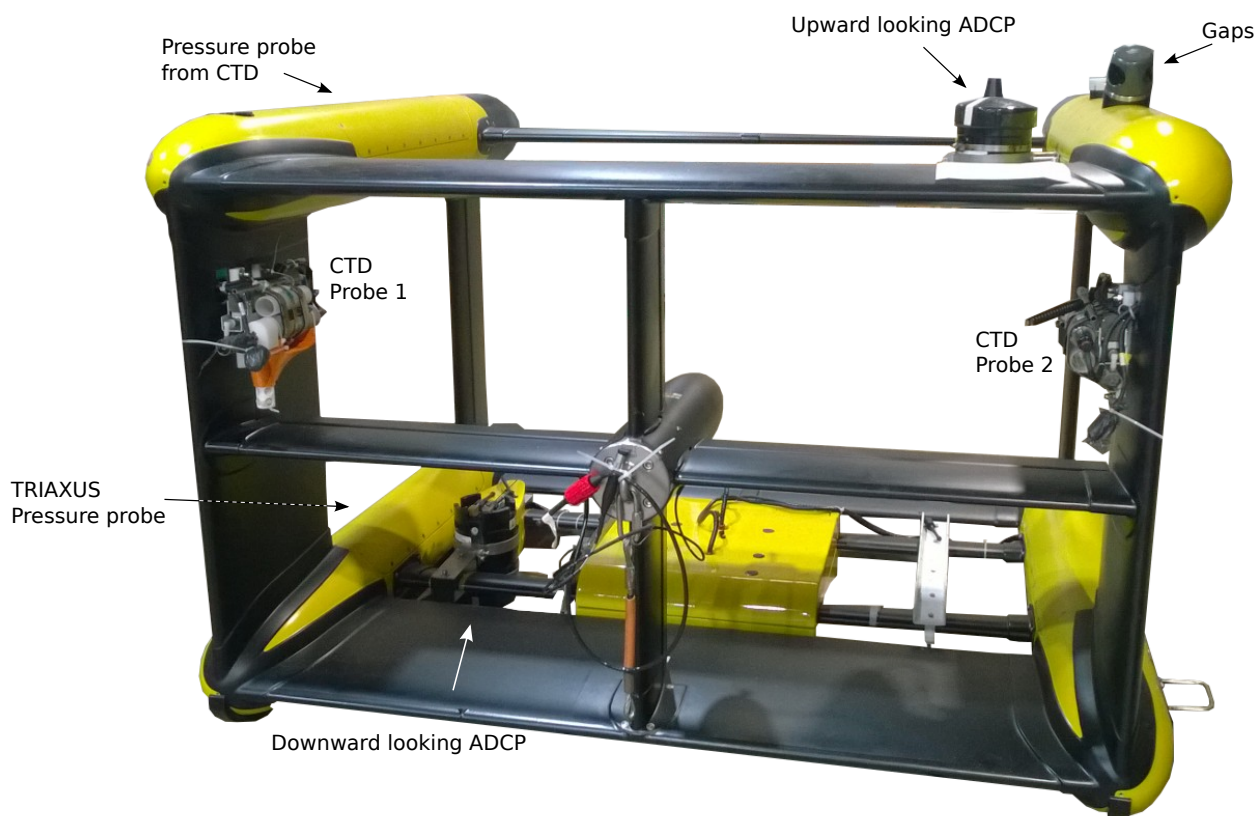
Figure 4: Setup of topAWI platform on 21 November 2018. The positions of the CTDs and pressure probes are indicated, as well as the upward and downward looking ADCPs and the GAPS system. Dimensions are 1.95 x 1.25 x 1.85 m for width, height and length, respectively (MacArtney Underwater Technology, 2019).

Sampling rates

Both the upward- and downward-looking ADCPs are made up of 4 slanted beams (slant angle θ = 20°) with an acoustic frequency of 1200 kHz and a central beam of 600 kHz. The latter was not used for the data acquisition of this study. The ADCPs were set up at a single ping sampling rate and with 13 bins of 1 m equally spaced from 1.66 to 13.66 m vertical (i.e. non-slanted) distance from the transducers. The actual measurement frequency of approximately 1 Hz is due to limitations of the electronics within the ADCP, which is significantly lower than its acoustic capabilities. The acoustic limitation in the water would permit a significantly higher measurement frequency. Indeed, the two-way travel time for a 15 m distance at an average sound speed in seawater of 1500 m/s is 0.02 s, allowing for a theoretical (acoustically limited) ping rate of a bit less than 50 Hz. In order to minimize the time used for the ADCP measurements and to be able to get the most information out of the data, no pre-processing was done during the data acquisition itself.

The Seabird CTD was sampling at a rate of 24 Hz, whereas pressure from the TRIAXUS vehicle was recorded at approximately 5 Hz. Finally, a 150-kHz ADCP from TELEDYNE RD Instruments was mounted in the hull of the ship at 11 m depth (VMADCP), measuring at a frequency of 0.5 Hz. The VMADCP time series were processed with the help of the "ossi" Matlab toolbox of GEOMAR. Its data was used as a reference for the ocean velocities.

2.2   Study site - Equatorial Crossing

The data used in this study was collected on an equatorial transect of the Atlantic Ocean from latitude 2°S to 2°N on the 24.05.2018 and 25.05.2018, as summarized in Table 2 and shown in Figure 5.

Table 2: Navigation details on the equatorial crossing transect.

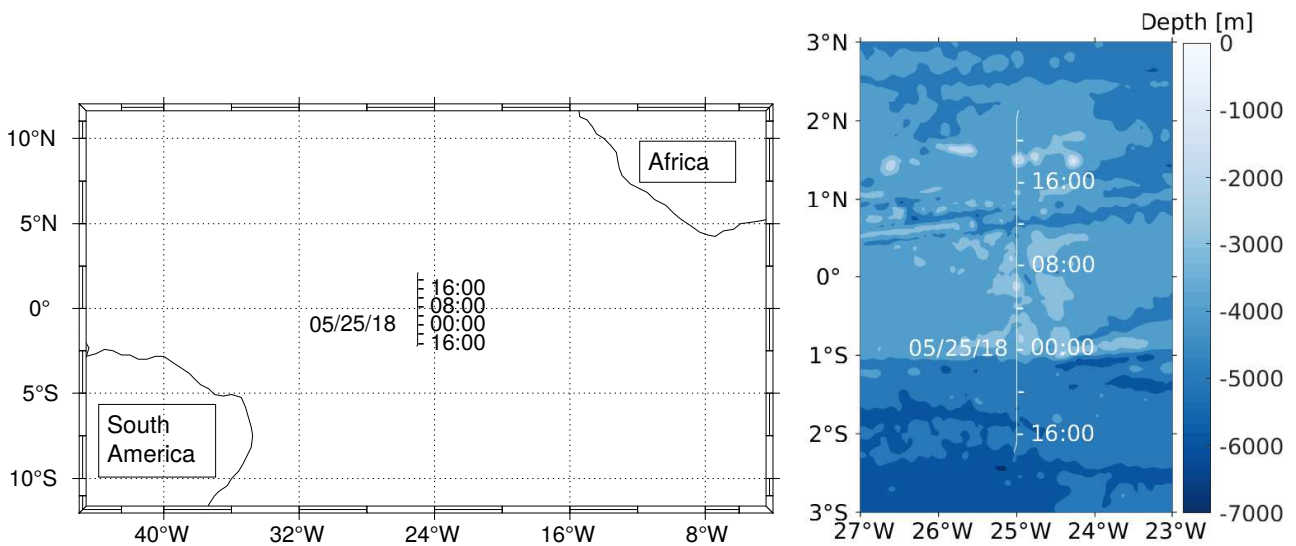| Dive	Equatorial crossing
UTC Start time [dd.mm.yyyy HH:MM]	24.05.2018, 13:47
UTC End time [dd.mm.yyyy HH:MM]	25.05.2018, 22:41
Start latitude/ longitude	2°14'10"S/ 25°01'26"W
End latitude/ longitude	2°07'50"N/ 24°58'49"W
Distance [km]	486
Average speed [kts] / [m/s]	8 / 4.1
Vertical undulation [m]	5-300

Figure 5: Equatorial crossing transect. Track between the 24.05.2018, 13:47 and the 25.05.2018, 22:41.

Figure 6 shows the sea surface temperature (SST) anomaly for the day when the equatorial transect of PS113 began. It shows a positive anomaly of approximately 1° C. From the data accessible on *https://www.ospo.noaa.gov/Products/ocean/sst/anomaly/2018.html* (NOAA Office of Ocean Exploration and Research, 2018), the anomaly was observable for the whole month of May and generally the SST anomaly was positive since the beginning of 2018. In their work, Góes and Wainer (2003) predict a weaker and shallower EUC in warm years.
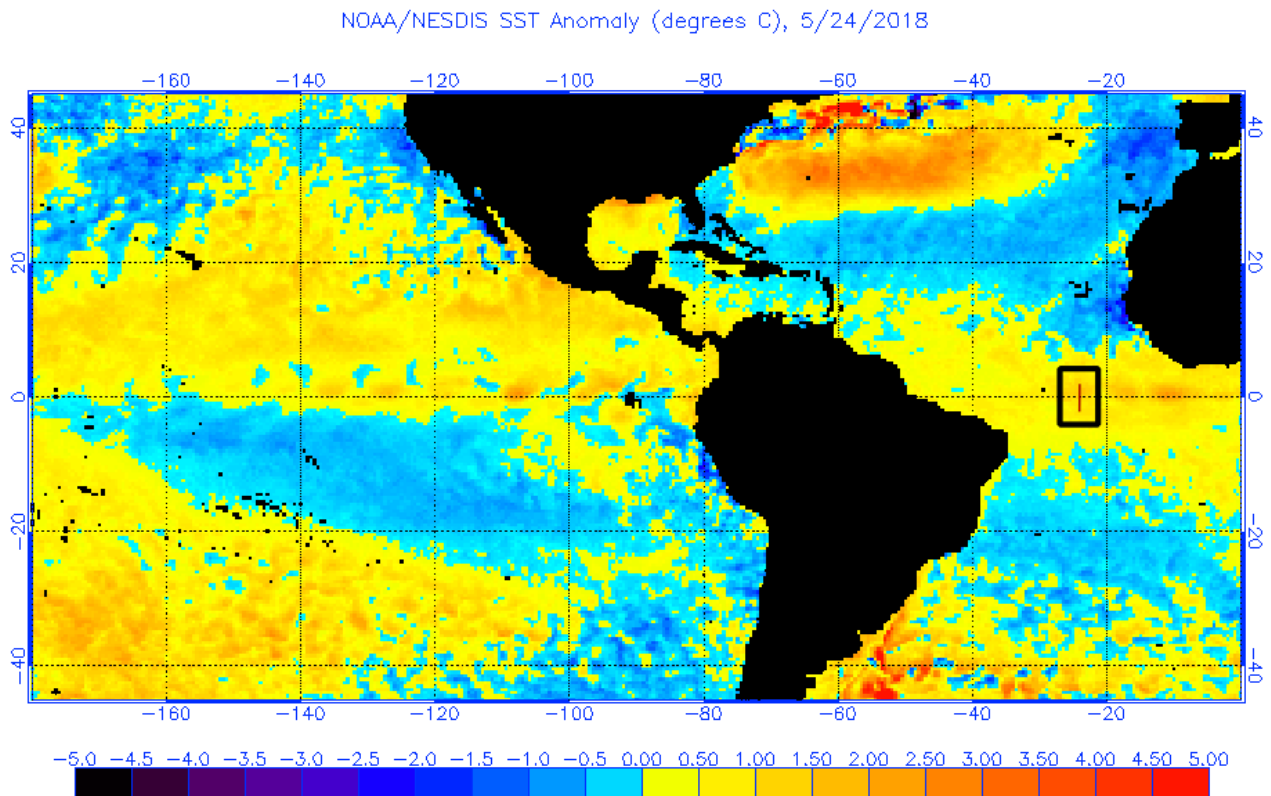
Figure 6: Sea surface temperature anomaly on the 24th of May 2018, (NOAA Office of Exploration and Research, 2018). It represents the actual sea surface temperature once its daily SST climatology has been removed. Positive values indicate a SST warmer than usual at this period of the year. The red line within the black square illustrates the location of the transect done in the scope of PS113.

Along the transect, the ship speed was kept almost constant around 8 knots (4.1 m/s). The undulations were taking place between the near surface and 300 m depth in a sawtooth profile requiring approximately 10 minutes for a total up- and downcast, for a total of more than 150 entire casts. The undulations can be seen in Figure 7. Most undulations were completed as planned, but roughly 7 did not return data over the complete undulation.
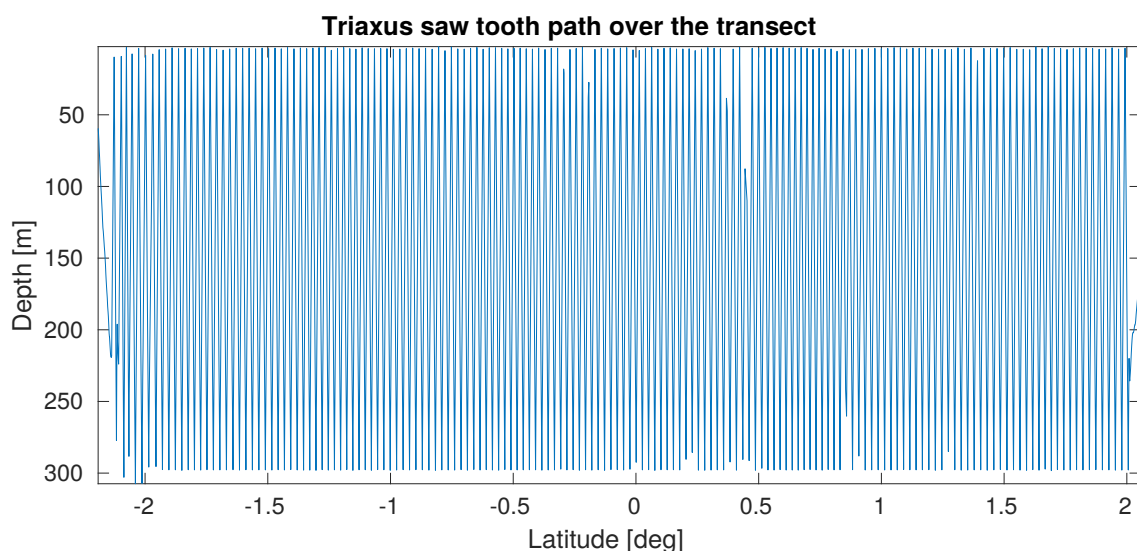

Figure 7: Saw tooth profile, with depth calculated from the topAWI CTD pressure sensor.

3 Methods

We now explain the steps needed to arrive at an estimate of ε. Many different data manipulation steps are required before the calculation of the structure function. Data treatment and processing were achieved with the software *Matlab*.

3.1 Preprocessing steps

The preprocessing steps aim to remove outliers. Several sources of error can be encountered. Whereas some are assumed to be negligible, such as sound absorption, interference by physical objects and vibrations (which make the use of conventional shear probes inappropriate), the relevance of others have to be carefully assessed, such as for random noise in single ping ADCP data or ship and TRIAXUS cable induced turbulence.

3.1.1 Timestep check

The topAWI system consists of 7 measurement devices plus the TRIAXUS flight control itself, also referred to as *vehicle* data. Each of those is connected to separate laptops and produce time series data. The computers are all synchronized with the ship's GPS supported master clock. Data was supposed to be merged in a common timestamp. However, for various software and hardware reasons, this was not always achieved on PS113. Therefore, parameters measured by more than one instrument can be compared to check and, if necessary, correct timestamp issues. For this purpose, the undulations provide prominent signals, in e.g. pressure or vertical velocity.

CTD and vehicle comparison

The first idea is to compare the depth obtained from the vehicle pressure probe with the CTD one. Both should differ by only approximately 1.25 m or less, based on the positioning of the probes in the vehicle (see Figure 4) and the inclination of the TRIAXUS. After a first visual examination, the times of maximal depth occurrence were compared.

For the equatorial crossing transect, a data loss event occurred on the 24.05.2018 at around 16:07 UTC and induced an offset in the CTD timestamp, which can be seen in Figure 8. This offset was determined by matching the lowest depths for each top-down cycle. The CTD offset was found to be approximately 20 seconds.
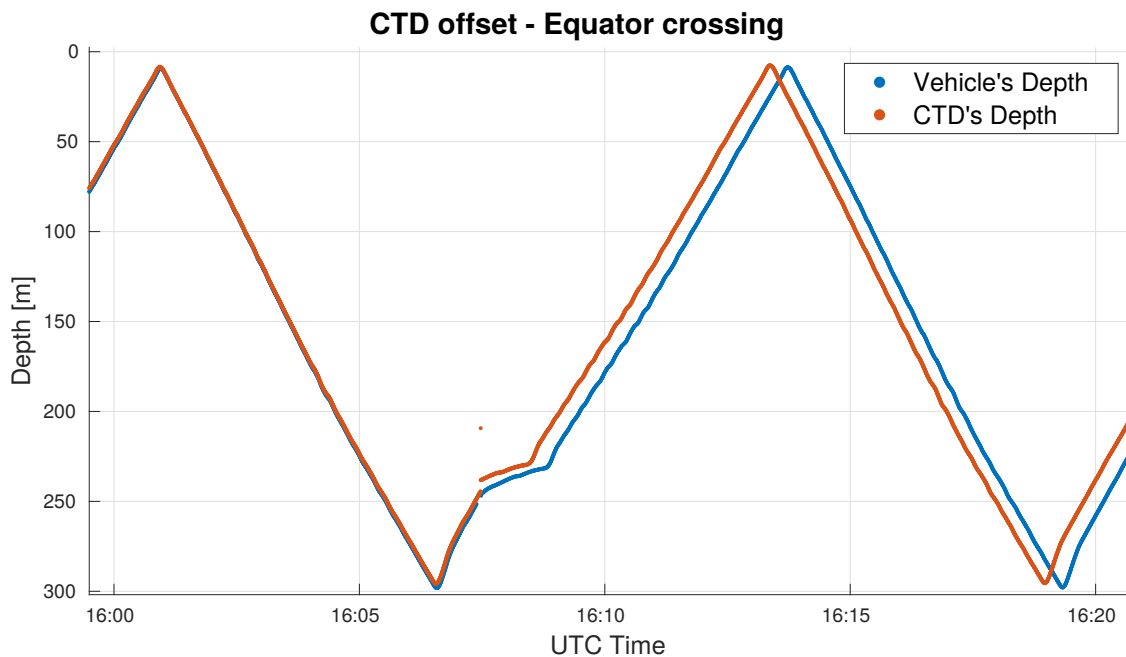
Figure 8: CTD offset issue for the equatorial crossing transect. The respective vertical velocities are shown in Figure 9.

ADCP offset

There were two types of issues with the ADCP data/timestamp. The first one was linked to a lot of data plotted at the same time (see Figure 9) and was resolved using instead the timestamp which records years as 4 digits, i.e. which is Y2K-compliant. The fact that this Y2K-compliant timestamp is recorded along with the commonly used non-compliant timestamp was only discovered recently. The method below deals with both this and the problem described next which is why we keep its description. The second issue is still remaining and is the presence of gaps in the data. These times without measurements were usually found right after the first issue of the wrong timestep. Figure 10 shows the remaining gaps.

Vertical velocities derived as the temporal derivative of both CTD and vehicle's depths were compared to ADCP measurements. The actual data acquisition rate achieved was of about 1 data point per second. It turned out that, on some occasions, the ADCP's velocities were similar with a slight offset to the other velocities. After investigation, the problem was linked to what happened on the screen on the ship: it seemed that the data was stopped for approximately 30 seconds displaying the same measurement and then showing within a few seconds a lot of new data - presumed to be taken at the same regular timestep, as the pattern is similar as can be seen at 02:53 or 03:04-03:05 in Figure 9. The data recording process was probably linked to this displaying issue and therefore these groups of points were written at almost the same time with the timestamp assigned there. The fact that these issues occurred shows that the ADCPs were not capable of working at a measurement rate of 2 Hz, which their specification claims is possible.
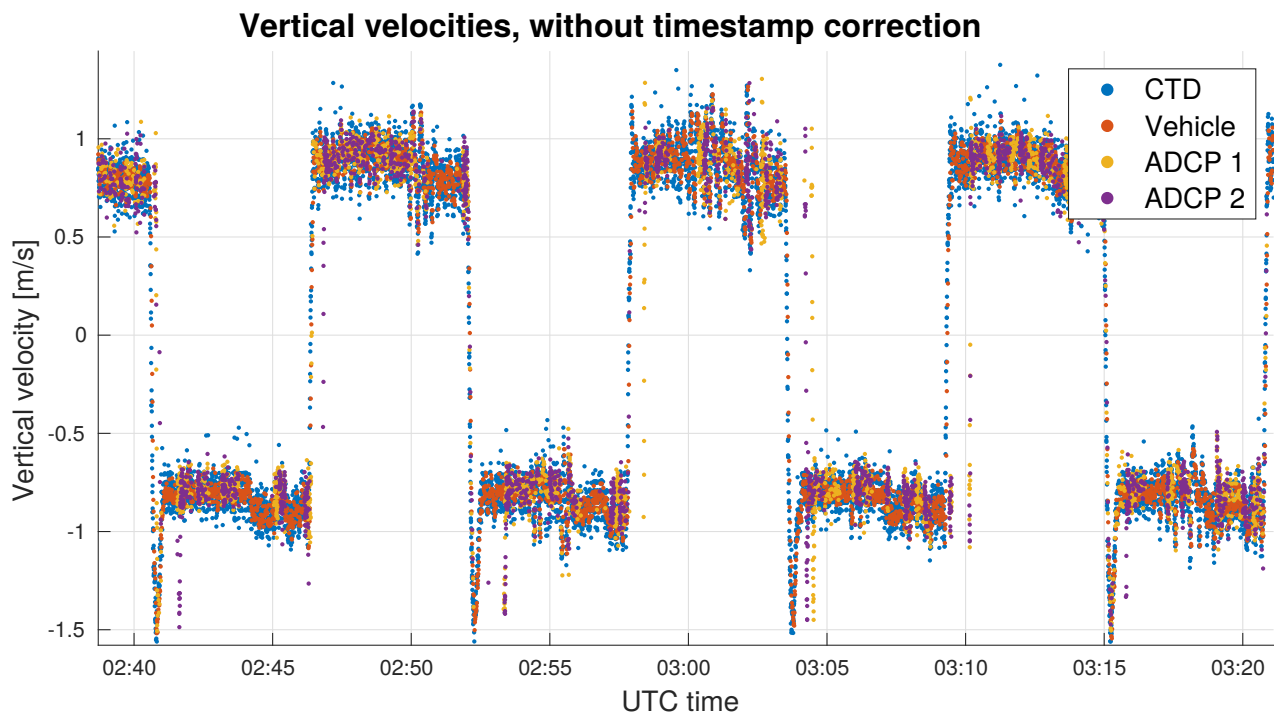
Figure 9: Vertical velocities from both ADCPs and from the derivative of the pressure records from both CTD and TRIAXUS (Figure 8). Data from both ADCPs are sometimes offset compared to the vehicle and CTD measurements.

To tackle the uneven time step issue, a data timestep interval between 0.9 and 2 s was considered as correct. The electronics in the ADCPs are known to not always take the same time for processing consecutive ensembles which likely explains why the timestep interval is not constant but changes slightly. Figure 10 shows the actual intervals, many with wrong cases exceeding the 2 s threshold. Trials were made to remove the value either just before, after, or both before and after a bad interval. All three solutions turned out to visually remove most of the offset problem by eliminating almost the same percentage of values. This fact brings evidence that all bad intervals were grouped. In the case of the equatorial transect, before the use of the Y2K-compliant timestamp, it represented 10.4% of the total values. Using this data would be possible only if we had a way to retrieve the actual time they were made. Various attempts to do this were unsuccessful. Therefore, only the 89.6% of data points with a correct timestep were retained from the non-Y2K-compliant timestamp. For the Y2K-compliant timestamp, all data can be used. Larger Δt remain, but the available data is ok.
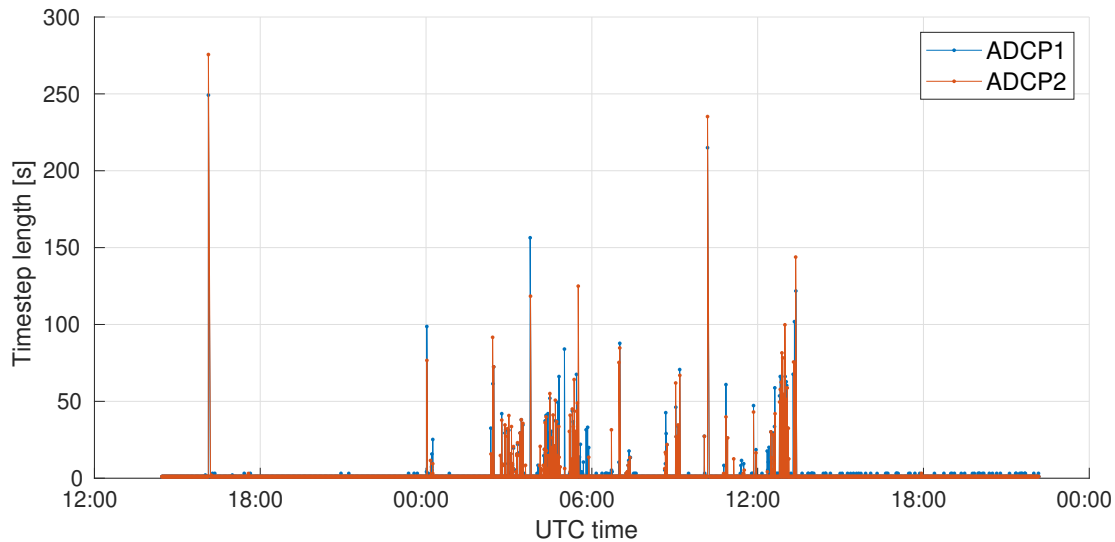
Figure 10: ADCP timestep interval in seconds over the whole measurements period. Note that the ADCPs were programmed to a timestep of 0.5 s.

Inclination

Since both the vehicle and the ADCPs have pitch and roll measurements, and since they are all fixed on the same rigid frame, their inclination should match and can be used as another indicator for timestep fitting. For small angles, it can be approximated as follows:

$$inclination \approx \sqrt{roll^2 + pitch^2} \tag{6}$$

The inclination was compared between vehicle and ADCP measurements. The resulting time series are shown in Figure 11. It is found that the ADCPs' inclinations are noisier than the vehicle's and that a systematic error based on the different positioning during up-/downcasts seems to contaminate the data. Nonetheless, their mean and variance appear to agree reasonably. Therefore, we conclude that the orientation of the ADCPs can be determined from the ADCP's sensors and the vehicle's sensor data does not need to be matched.
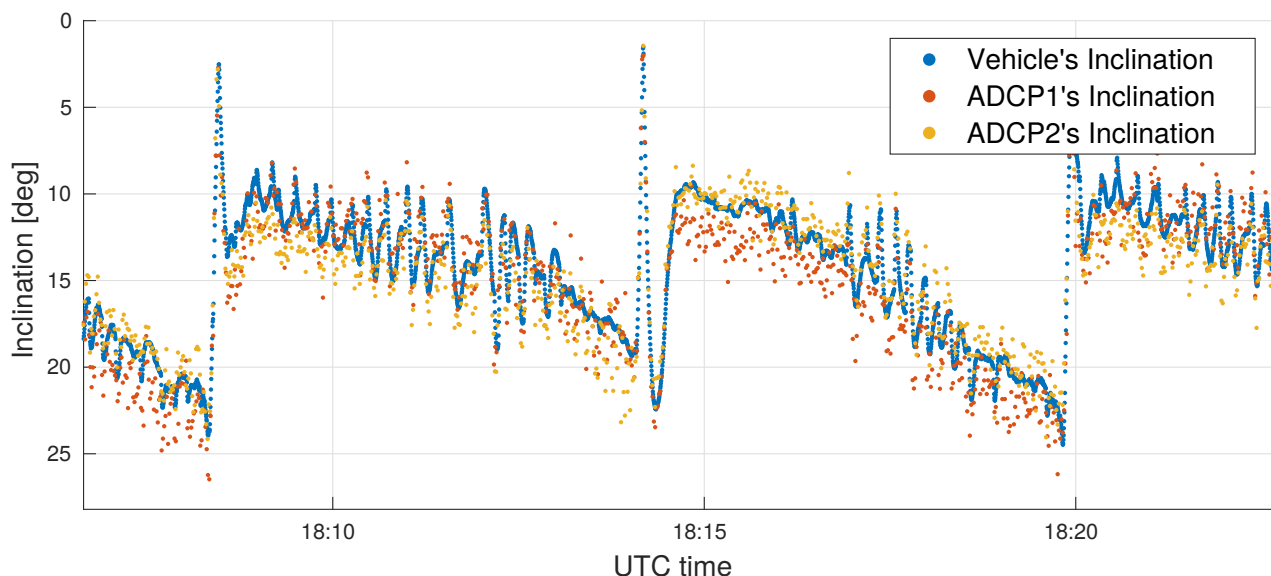

Figure 11: Time series of approximate inclination from the vehicle data and the ADCPs.

Depth comparison

Then, as a last timestep check, the ADCPs' measurements of vertical velocities were integrated in time to get depth and compared to the other measurements. Obviously, because of the gaps generated by the offset issue and the lower sampling rates of the ADCP, the depth (Figure 12) obtained by the ADCP is not meaningful, but it's pattern is and the peaks match.
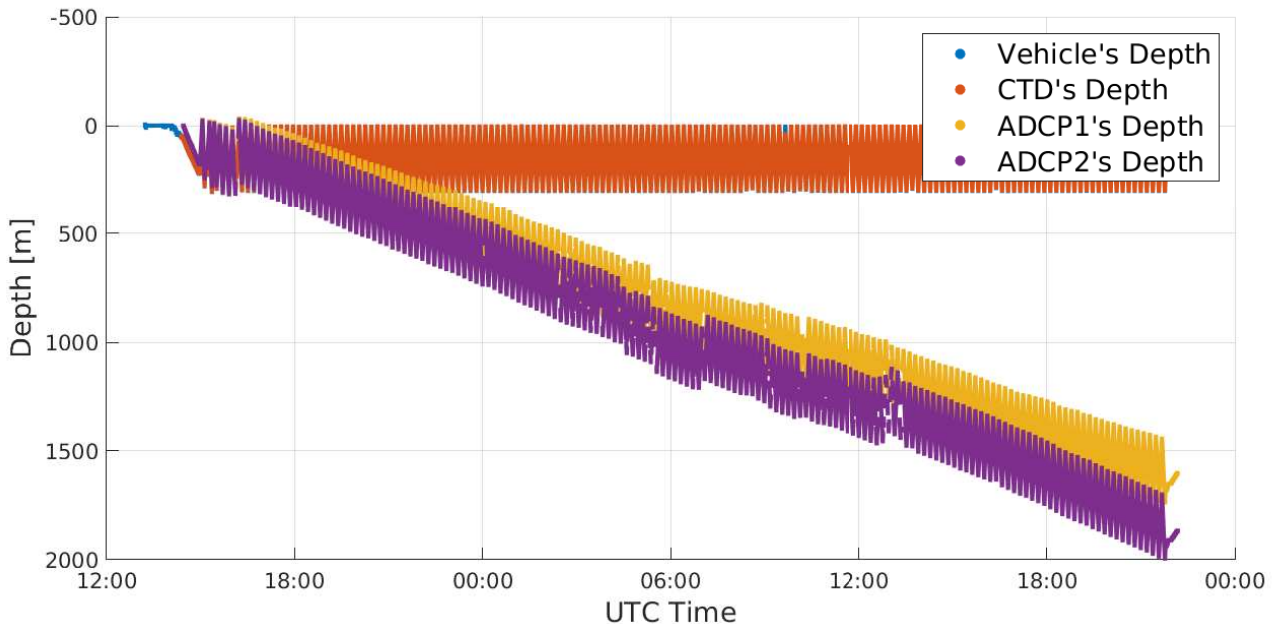

Figure 12: Time series of depth from the pressure sensors and from the integral of the vertical velocities from the two ADCPs.

Nonetheless, the amplitude of the undulations is matched very well indicating that the amplitude of the vertical velocity measured by the ADCP is correct

In order to get the real depth of the ADCPs, an interpolation of the CTD depth to fit each ADCP's timestep was then applied. The nearest neighbours method was used in order to not introduce any values not already in the original time series.

3.1.2   Vehicle positioning

A GAPS system is mounted on the topAWI platform in order to provide the absolute position of the vehicle. However, the receiver at the hull of the ship couldn't be deployed for ship velocities exceeding 6 kts, because its fixation would be prone to damage due to turbulence. For the transect examined in this work, no positioning data was available. Therefore, some rough assumptions were made in order to approximate the location of the platform in comparison to the one of the ship. The difference in latitude was calculated as if the cable length was tightened in a straight line behind the ship, including basic geometric considerations to account for depth. Since the course of the ship was due north during the transect, we assume that the ship's longitude equals the topAWI's longitude at each time step.

3.1.3   Range

Different pitch and roll values of the ADCP lead to the fact that the same bin from different beams measures in different vertical distances above/below the ADCP. To tackle this issue, one has to

account for the range. This allows determining the actual depth of each measurement bin.

To know the depth of the bin, one needs to multiply the range with the purely vertical range of an upright ADCP, i.e. not tilted. This is what is set in the instrument programming as bin size (named WS command for the ADCP TELEDYNE RD Instruments), and not the actual along beam distance. The difference between them is visualized in Figure 13. From the geometry, it follows for the case used here:

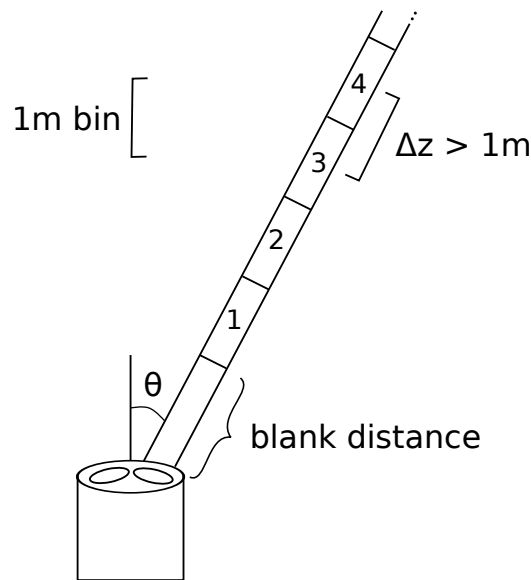$$\Delta z = \frac{1\ m}{cos(20°)}\ . \tag{7}$$

Figure 13: Schematic of the ADCP bin depth, with Δz the actual along beam range of the bins compared to the vertical upright range of 1 m bins. For the ADCP used here, $\theta = 20°$.

3.1.4   Compass deviation

The magnetic poles of the Earth are moving slowly ($\approx$ tens of km per year) and the total magnetic field at any point on Earth, therefore, depends on time, latitude, longitude and elevation. Such oscillations lead to magnetic declination, i.e. the angle between where the magnetic field points and the geographic north. A way to account for it is to use the International Geomagnetic Reference Field (IGRF) function from Thébault et al. (2015) which predicts the magnetic field for the next few years based on data acquired until 2015. For the equatorial transect, we assume a constant time, longitude and height, and only interpolate between latitudes.

3.2   Earth velocities

First, the ADCP measured velocities need to be transformed from beam to earth coordinates to get the eastward (U) and northward (V) components. This step is implemented following the ADCP Coordinate Transformation guide from Teledyne RD Instruments (RD Instruments, 1989) as coded in the Matlab function *beam2earth.m* written by Wilken-Jon von Appen.
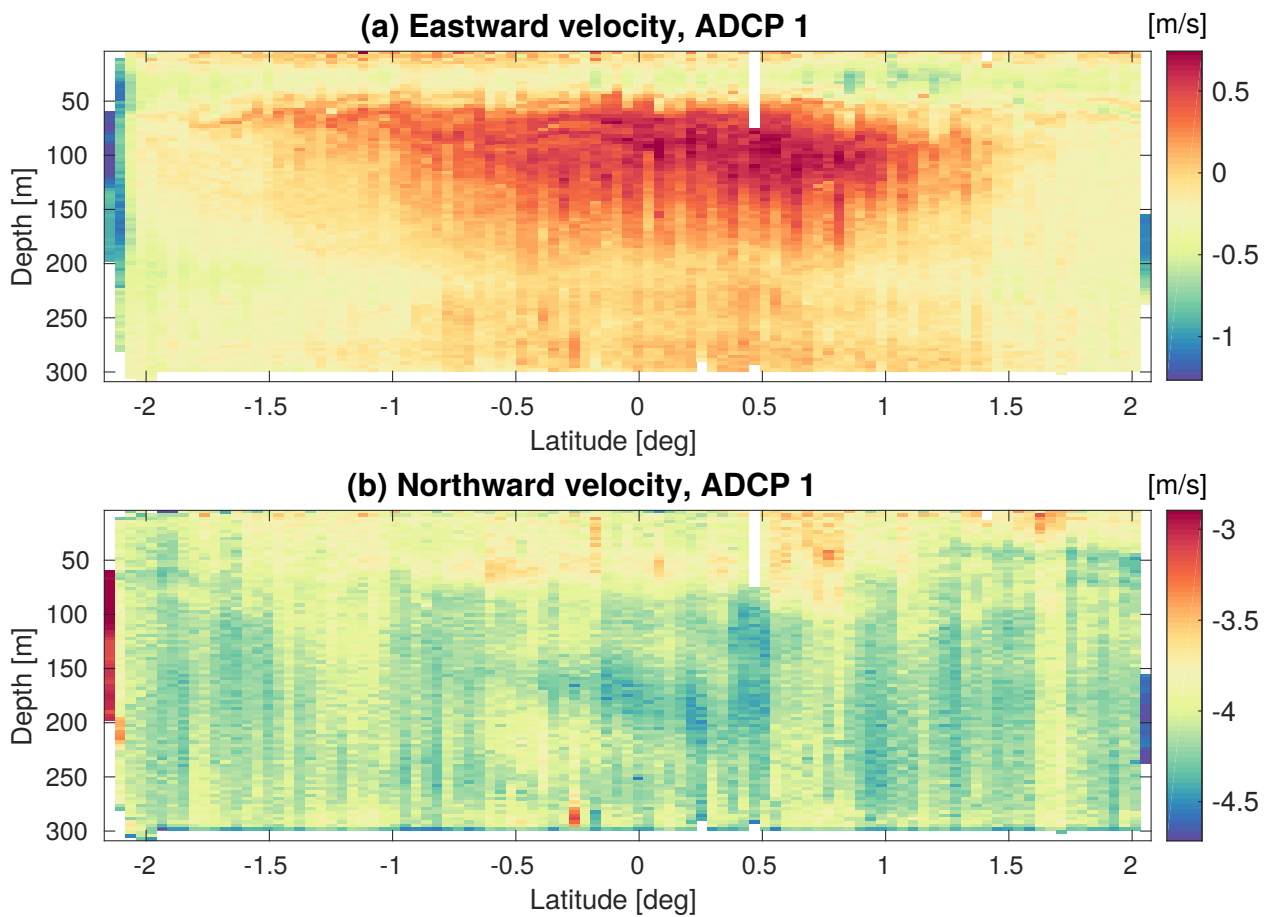
Figure 14: Eastward (a) and northward (b) velocities from the upward looking ADCP only. ADCP 2 shows similar patterns. Compass correction was applied, but the ship speed was not removed.

The ADCPs on the TRIAXUS measure the velocity of the ocean water with respect to the ADCP. This is the ocean velocity with respect to ground minus the instrument's motion, which in turn is the ship's velocity over ground plus the undulation induced motion.

Figure 14 shows an early stage of the velocity profile processing. One can see that the velocity pattern seems plausible, but the values for the northward velocities are extremely negative. This feature agrees with the fact that the main velocity in this direction applied on the TRIAXUS is the one of the ship. Indeed, the latter was moving with an almost constant velocity of 4.1 m/s northwards, which is detected as a big southward ocean velocity from the ADCP point of view (light green colors in Figure 14 (b)). Also at the beginning and the end of the transects, there are some areas with high velocities due to the deployment and recovery of the platform. Such manipulations require great diligence (see also Figure A3) and the velocity data during those times cannot be used.

The next processing step will be to remove the ship velocity from both northward and eastward components. For this purpose, a 15-min Butterworth lowpass filter is applied on the raw ship velocity, which is then added to the ADCP velocity estimates.

Finally, we would need to remove the undulation induced motion. It wasn't done for this thesis because we assume that the effort required to estimate these motions without any information from the GAPS system would be a significant investment compared to the improvement of the profiles that one could expect.

3.3   Method for dissipation of TKE

This method relies on numerous assumptions. First of all, the very principle of ADCP measurements relies on the fact that scatterers flow with the same velocity as the water (RD Instruments, 1989). Secondly, one of the most crucial hypothesis is to assume that for a certain time – which also translates into a space scale for the towed system – the system is ergodic. It means that due to its homogeneity and stationarity, the system has the same behavior (statistical quantities of the system are constant), being averaged either over time or over distance. The latter has to be chosen in order to be sufficiently big to have a meaningful average, i.e. containing enough individual measurements, but at the same time be small enough for the assumption of ergodicity to be appropriate. We know that the system statistics will change over a certain horizontal and vertical distance. However, if the horizontal distance is sufficiently small, the system will not have changed for estimates at the same depth from neighbouring undulations. Therefore, in this work, we average over bins of Δz = 10 m depth and Δy = 0.1° latitude. Tests with somewhat smaller or larger bins did not change the results significantly.

Finally, the last hypothesis is that the Reynolds decomposition can be applied for the along beam velocity u, namely:

$$u = u' + \bar{u}\,, \tag{8}$$

with u' being the random high-frequency motions due to turbulence and $\bar{u}$ the temporally and vertically averaged velocity in the box. Since the influence of the TRIAXUS motions should be the same for each bin of a beam, this part is expected to end up in the mean ($\bar{u}$) as well.

Steps

For each possible distance r between bins, and at each depth z, the n-th order structure function D can be calculated using the along beam velocities:

$$D_n(z,r) = \overline{[u(z) - u(z+r)]^n} = \overline{[u'(z) + \bar{u}(z) - (u'(z+r) + \bar{u}(z+r))]^n} \tag{9}$$

If we assume that $\bar{u}(z) = \bar{u}(z+r)$ (we return below to whether this assumption is appropriate), this simplifies to:

$$D_n(z,r) = \overline{[u'(z) - u'(z+r)]^n} \tag{10}$$

Note that for small r, more estimates can be obtained. For example, the difference between bin 1 and bin 2, as well as between bin 12 and bin 13, and all the combinations in between can be used for r = 1 bin. Whereas only the difference between bin 1 and bin 13 can be used for r = 12 bins. For both D_2 and D_3, all the estimates within a single grid box are then averaged to get only one value per grid point. Indeed, because turbulence is formed of many small random motions, every single measurement will contain a random value. Averaging over multiple measurements should yield a reproducible statistic.

The second order structure function gives the following relationship to dissipation (Wiles et al., 2006):

$$D_2(z,r) = C_v^2 \varepsilon^{\frac{2}{3}} r^{\frac{2}{3}} \tag{11}$$

with ε being the dissipation and C_v^2 an experimental constant found to be between 2.0 and 2.2 (Wiles et al., 2006). Horwitz and Hay (2017) also showed that the third order structure function can be used to retrieve ε without requiring an experimental constant using the formula:

$$D_3(z, r) = -\frac{4}{5}\varepsilon r \tag{12}$$

After fitting respectively the observed averaged second and third order structure functions for each grid point $\Delta y \, \Delta z$, Equations 13 and 14 can be solved for the dissipation for each r value to get one estimate of ε from D_2 and one from D_3.

$$D_2(z, r) = a_2 r^{\frac{2}{3}} + b_2 \qquad \Rightarrow \qquad \varepsilon_2 = \left(\frac{a_2}{C_v^2}\right)^{\frac{3}{2}} \tag{13}$$

$$D_3(z, r) = a_3 r + b_3 \qquad \Rightarrow \qquad \varepsilon_3 = -\frac{5}{4}a_3 \tag{14}$$

During the coding part of this work, a few plots were made to investigate the validity of the D_2 and D_3 estimates. In Figure 15, the second order structure function for a particular grid point is shown. As was shown in Equation 11, the function should follow a curve shape to the power of 2/3. Instead of that, a squared relationship is observed. One could argue that it could be the remaining mean shear component, which being squared in the structure function would lead to this particular shape. Therefore, the following method has been tested, in order to remove the shear component.
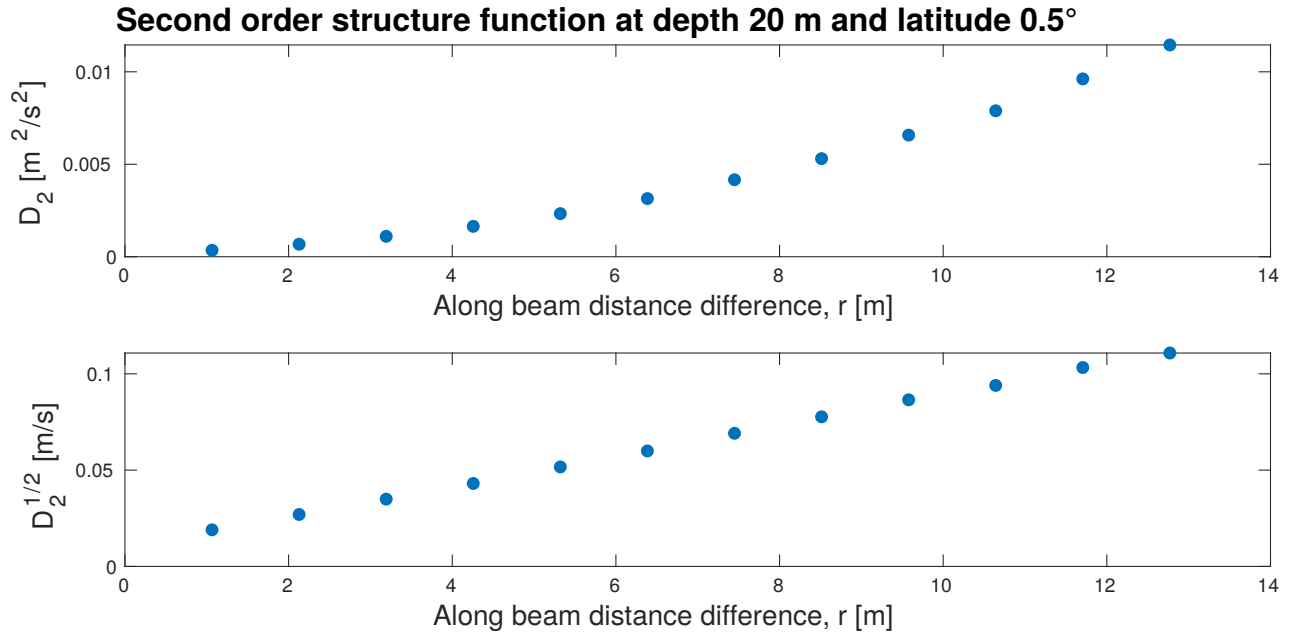

Figure 15: Observations for the second order structure function D_2 and the square root of it. The estimate is valid for the box of depth = 20 ± 5 m and latitude = $0.5 \pm 0.05°$. For larger r, the uncertainty on the value of D_2 becomes bigger due to fewer estimates.

In order to calculate the shear, one first needs the velocities in earth coordinates. The transformation is made as previously explained in Section 3.2. The second step is to average the U and V velocities into a grid of dimensions Δy, Δz, in this case $\Delta y = 0.1°$ lat, $\Delta z = 10$ m.
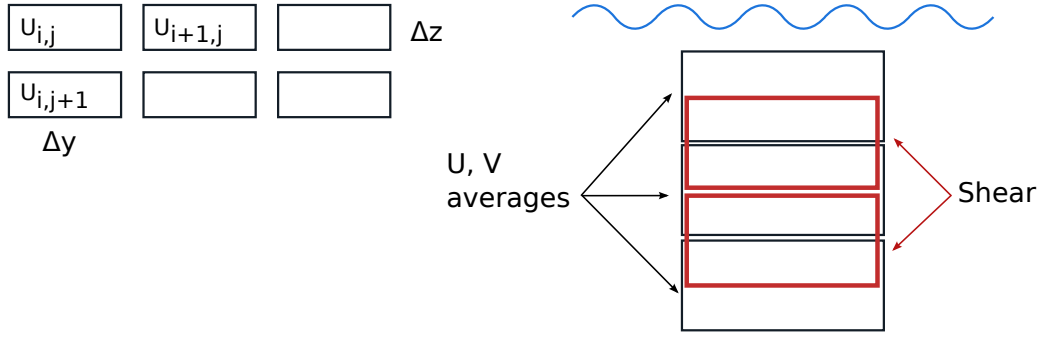
Figure 16: Positioning of the shear calculation boxes, staggered to the grid used for velocity averages.

The vertical derivative gives then the shear for each velocity component (U = eastward velocity, V = northward velocity). It is computed with Equation 15 for each middle point of two velocities, resulting in a staggered grid as shown in Figure 16.

$$\frac{\partial U}{\partial z} = \frac{U_{i,j} - U_{i,j+1}}{\Delta z} \tag{15}$$

These obtained shear values need to be multiplied by the depth of each respective bin to get $\tilde{u}, \tilde{v}$ average values, i.e. the component due to vertical shear for each bin of the ADCPs. Then those have to be transformed back to beam coordinates. This is done using the reverse four beams transformation, assuming that both the vertical velocity and the error velocity are equal to 0. Finally, the shear components can be taken out from the D_n estimate as shown in Equation 17 to allow new fits for ε. The effect of this correction will be assessed in the following section.

$$u = u' + (\tilde{u} + \bar{u}) \tag{16}$$

Starting from Equation 9 and inserting Equation 16 yields to:

$$D_n(z, r) = \overline{[u'(z) + \bar{u}(z) + \tilde{u}(z) - (u(z+r) + \bar{u}(z+r) + \tilde{u}(z+r))]^n}$$
$$= \overline{[u(z) - u(z+r) - \underbrace{(\tilde{u}(z) - \tilde{u}(z+r))}_{\text{mean shear component}}]^n} \tag{17}$$

Next, we use the staggered grid estimate of the shear such that shear contribution from D_n can be removed. The results of this method will be compared to the one without shear correction to assess its outcome.

4 Results

First presented below is the whole applied method. After an overview of the transect acquired with the mean of the CTD probes, the technicalities about the elaboration of velocity profiles are discussed in details. Then the EUC transport is estimated from the eastward velocity profiles. Finally, the result of the TKE dissipation rate ε calculations using the second and third structure function method are presented.

4.1 Method development

The following method was developed based on the successful attempts of Wiles et al. (2006) and Horwitz and Hay (2017) to estimate the turbulence from ADCPs using the structure function. A similar version was first implemented and led to the new shear calculation steps in the process, as explained in Section 3.3. The whole processing steps are depicted in Figure 17.
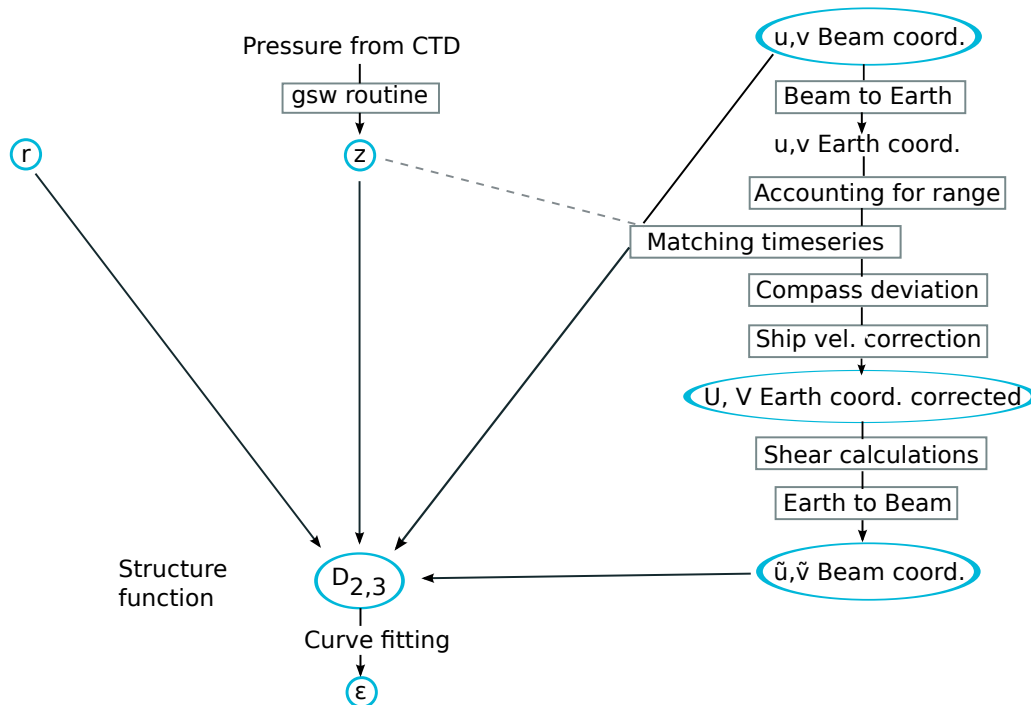

Figure 17: Flowchart illustrating the processing steps to obtain U and V in Earth coordinates for velocity profiles and the structure function D value to estimate the dissipation ε. Inputs (marked by blue ovals) are: a user-defined range of distances r, a pressure time series z (here from the CTD probe) as well as beam coordinates velocities u, v from the ADCPs.

In the case of a tethered ADCP, the structure function method has the considerable advantage of being able to deal with beam coordinate velocities directly. Indeed, since the vehicle motion induces the same component to all bins of each individual beam, it will be efficiently removed by the calculation of the structure function D (see Equations 9 and 10). Averaging it for all beams and bins and for all timesteps within each point of a latitude-depth grid will then, in turn, be an essential step to get a meaningful ε estimate. However, it is important to realize that the method requires already checked data for CTD pressure and U, V velocities in beam coordinates.

4.2   Interpretation of Equator Crossing

4.2.1   Hydrography, stratification and inertial subrange

To first get an idea on the location and main features of the EUC in this transect, a few variables from the CTD probe were depicted on a grid of Δz = 3 m and Δlat = 0.04 lat (i.e. 4.4 km) using the *twodstats.m* Matlab function of JLab (Lilly, J. M., 2017). Each point of the grid represent the mean values of approximately 150 to 500 point measurements within the box. Salinity is represented as a function of depth and latitude in Figure 18 (a). It ranges from values of 35.2 g/kg at 300 m depth, up to 36.8 g/kg at a depth of 60 m. Above this salinity maximum, the surface is again less saline. Already noticeable is the fine horizontal resolution achieved with the platform. Because it is known that the EUC is associated with a local maximum in salinity (Claret et al., 2012; Blanke et al., 2002), this plot already indicates the location of the current. Indeed, according to Figure 18 (a), the core of the EUC lies probably around 60 m depth. As will be seen later, the EUC acts as a net eastward transport of salinity. This transport takes place already from the western part of the basin (Stramma et al., 2005).

Potential temperature is shown in Figure 18 (b). It ranges from 11°C at 300 m depth to 28°C at the water surface. In turn, the potential density anomaly extends from less than 23 kg/m^3 to approximately 27 kg/m^3 below 150 m, as shown in Figure 18 (c). As the potential density of the ocean mainly depends on the temperature and salinity, one can observe in this case a stratification based on the temperature gradient. Moreover, there is a slight decreasing salinity gradient to be observed at the surface from south to north. Potential temperature and potential density anomaly gradients, both decreasing northwards, are also found at the surface. Such a configuration could be caused by the higher precipitation in the north, due to the ITCZ location, whereas evaporation is more pronounced in the south. As shown below, the high stratification goes along with a high shear zone between the depths of 50 and 80 m. This fact explains why the salinity maximum spreads a lot more on the longitudinal axis than on the depth axis.
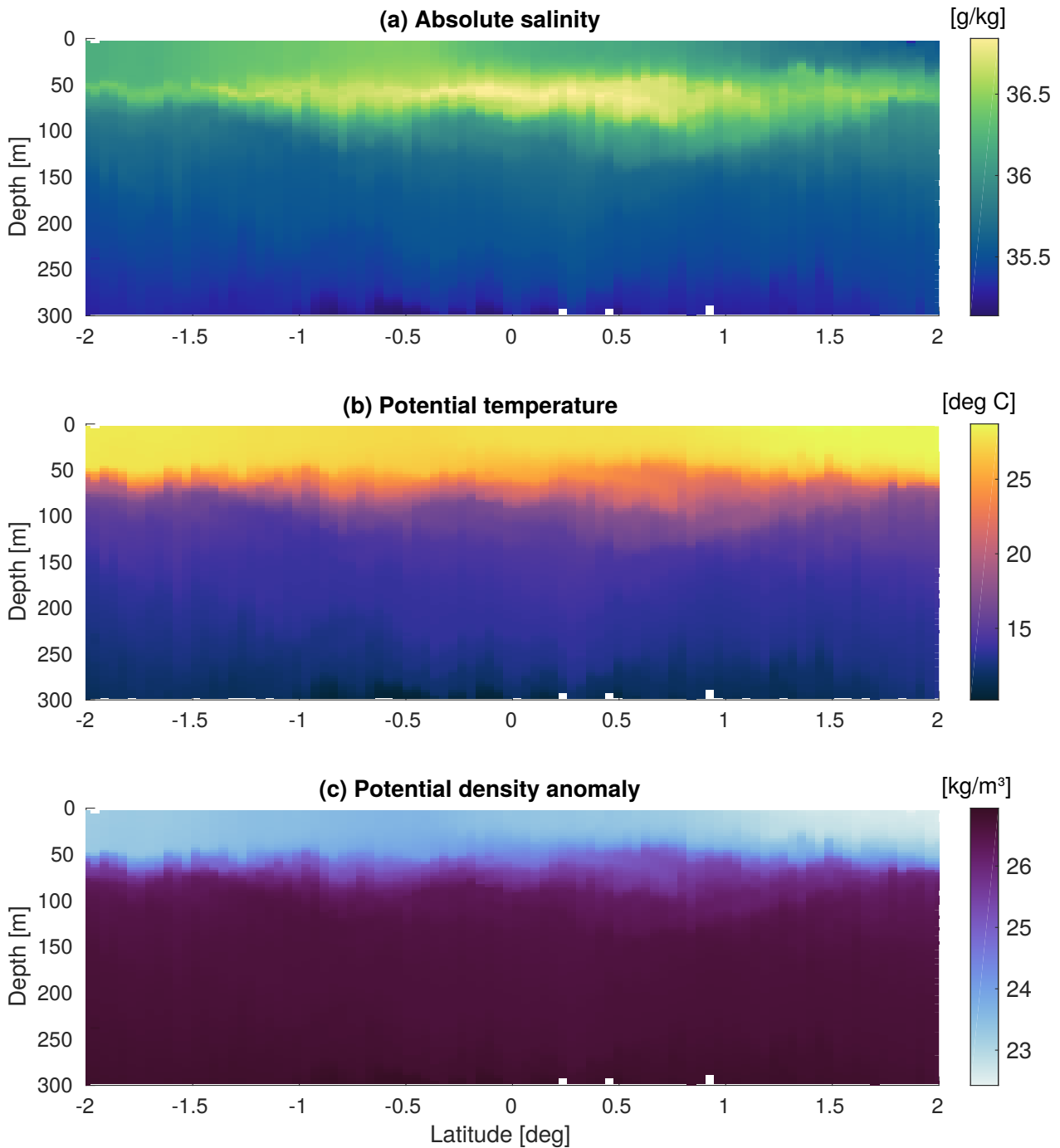
Figure 18: Transects from the topAWI CTD probe data of (a) Absolute salinity, i.e. the mass fraction of dissolved ions in seawater, (b) Potential temperature θ, i.e. the temperature a water parcel would have if adiabatically (without heat or salinity exchange) raised to the surface, and (c) Potential density anomaly σ_θ, i.e. the density a water parcel would have if adiabatically raised to the surface, with $\sigma_\theta = \rho_\theta - 1000 \text{ kg/m}^3$, where ρ_θ is the potential density.
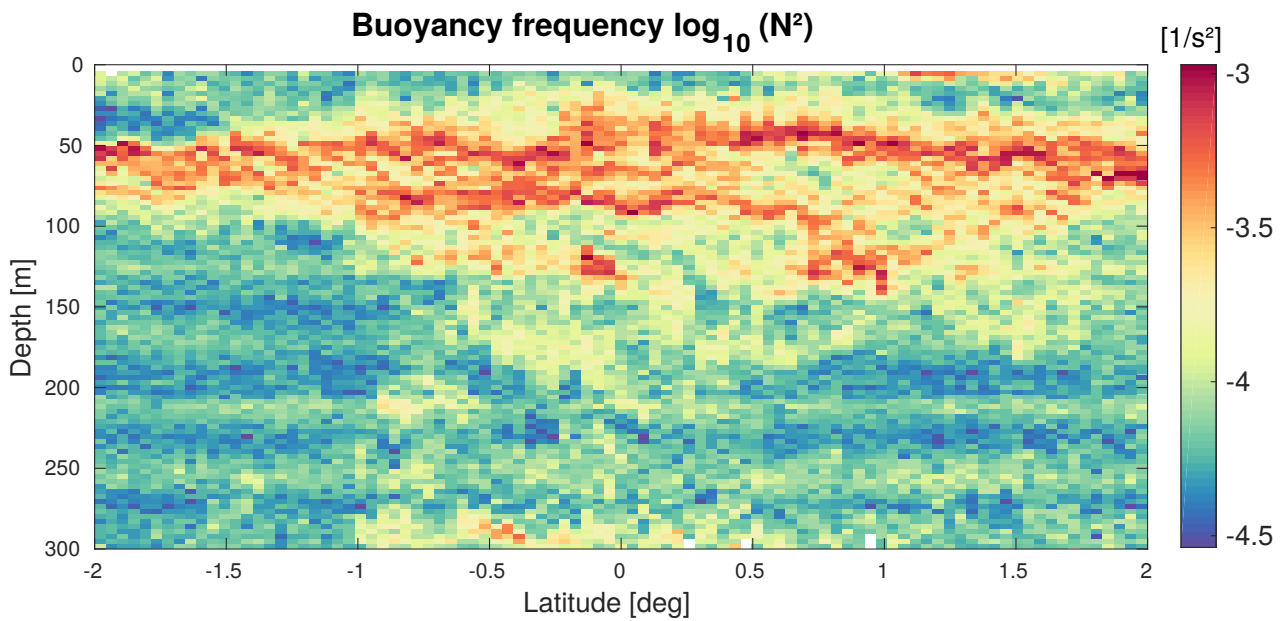
Figure 19: Logarithm of the buoyancy frequency squared, N^2, calculated with the *gsw* Matlab routine.

Figure 19 shows the distribution of the buoyancy frequency squared, N^2, over the equatorial crossing transect. In this particular case, high values of N^2 are distributed over a whole area, while in other parts of the ocean, a line due to a steep thermocline is a more typical pattern. These high values mean that the stratification is stable.

Because the structure function method applies only within the inertial subrange, which limits are defined by the Kolmogorov and Ozmidov scales, we calculate now its expected limits. The Kolmogorov scale can be calculated with Equation 4, admitting a kinematic viscosity of $\nu = 10^{-6}$ m^2/s and using the estimates of the expected dissipation rate from Table 1, i.e. 10^{-7} to 10^{-6} W/kg. The calculation gives a range for Kolmogorov scale between 0.001 and 0.002 m, which is smaller than our bins.

In turn, the Ozmidov scale is given with Equation 5 and using values from $10^{-4.5}$ and 10^{-3} s^{-2} for the buoyancy frequency squared (as taken from Figure 19). The scale is found to vary between 0.01 and 2.4 m. Again, these values are calculated from estimates, and whereas the 12 m value of r is too large based on these estimates, the first values of r are potentially within the inertial subrange, and the method could be applied using these points only.

4.2.2   Velocities

For the plots of the velocity profiles, the following technicalities had been used. First, a 15-min Butterworth low pass filtered ship velocity was removed. The first 5 m of measurements at the water surface were removed, due to contamination of the upward looking ADCP with sea surface signal. Depth is derived from the CTD pressure probe. Latitude comes from the vessel GPS. The cable length was removed from it, including the basic geometry of the cable inclination with depth. The fact that the cable was not straight behind the ship was not taken into account here, nor was the fact that it was not straight in the water. Therefore, undulation induced motions are still contaminating the data. Finally, the very beginning and end of the transect are removed, because of their specific movements linked to the deployment and the recovery.
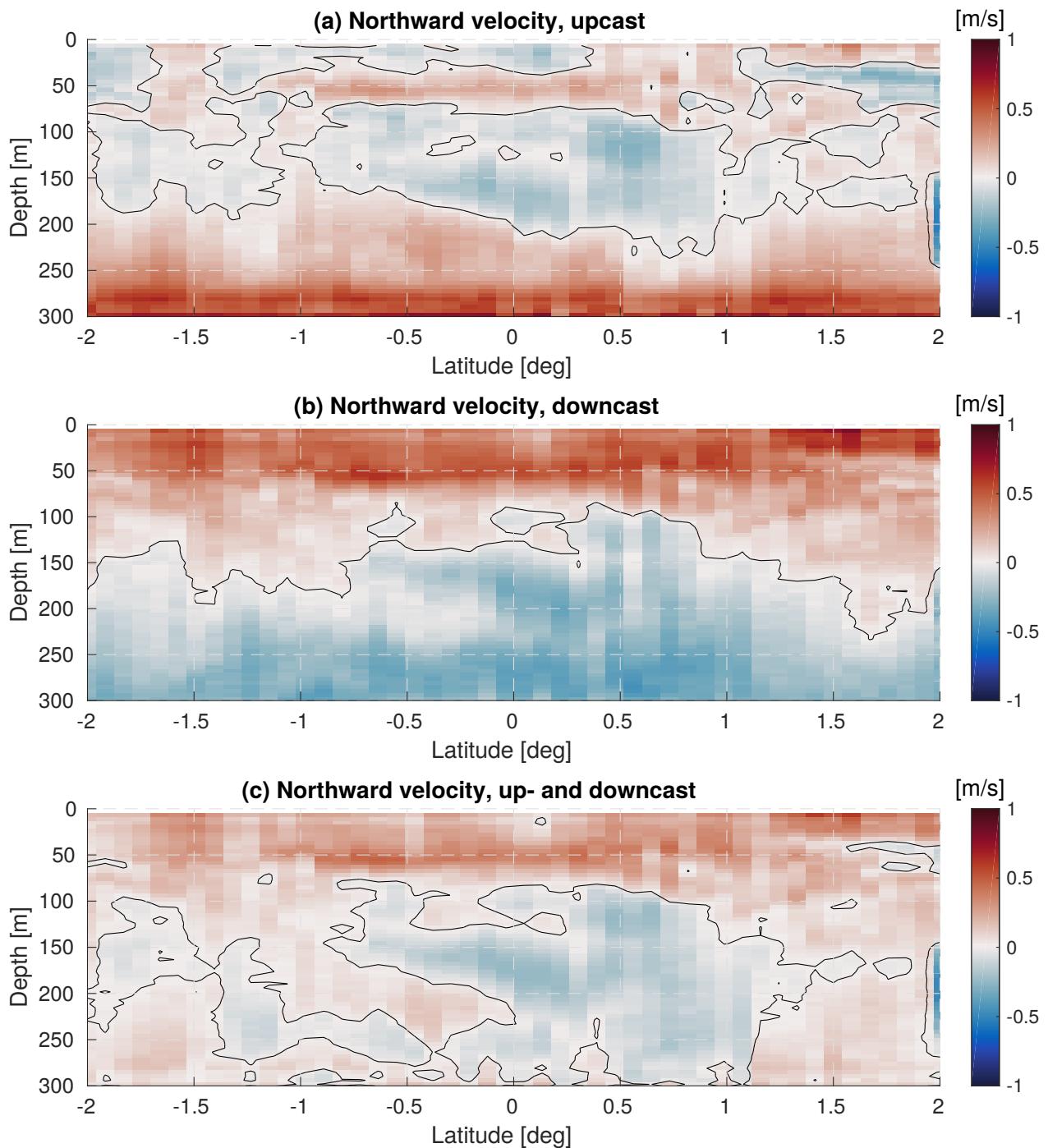
Figure 20: Transects of the measured northward velocities from a combination of both up- and downward looking ADCPs on topAWI. (a) is only based on data from upcasts, (b) only on downcasts, and (c) combines data from up- and downcasts based on the number of estimates from each. A black contour line shows here the zero velocity.
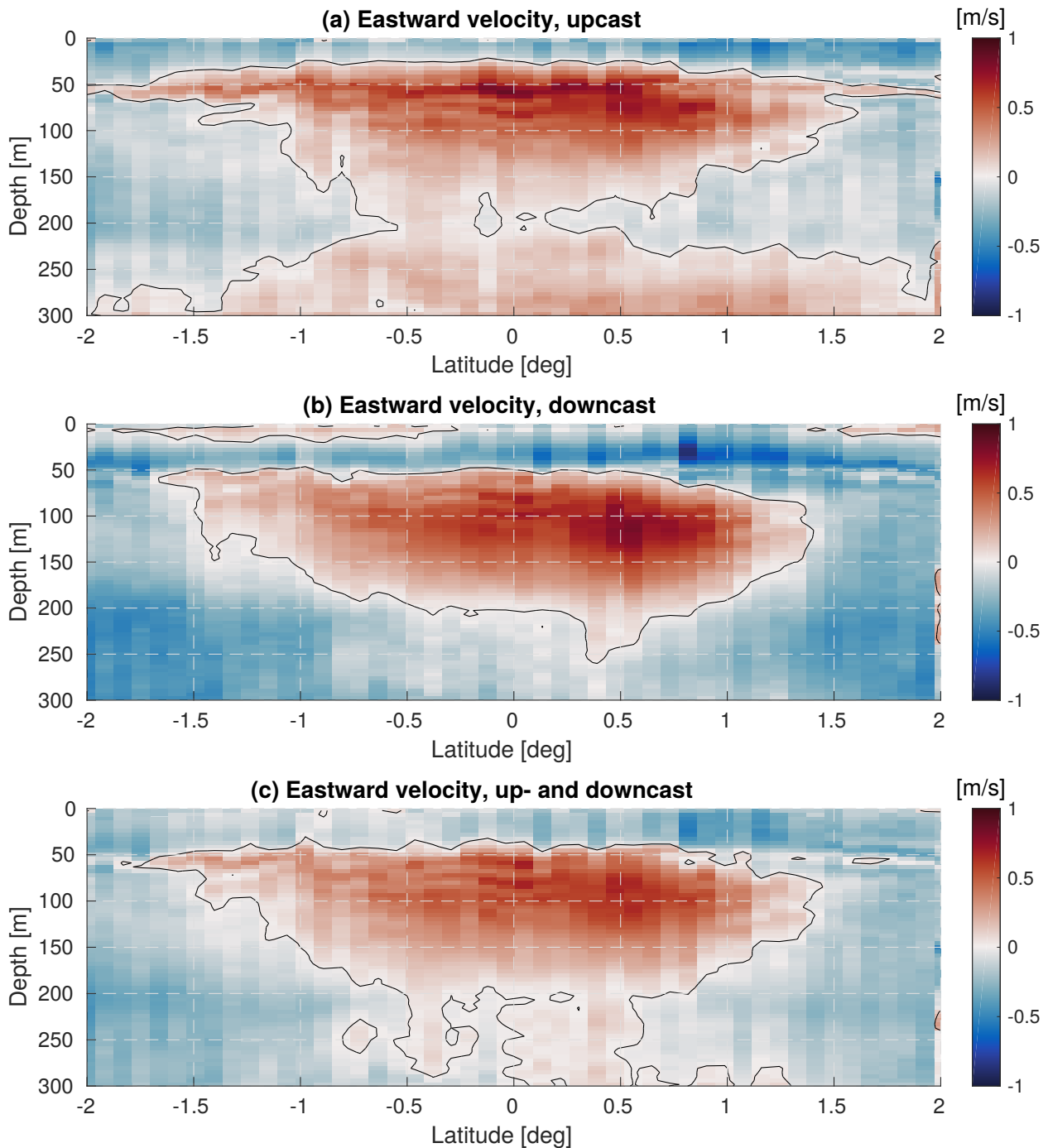
Figure 21: Same as Figure 20, but for the eastward velocity.

Figures 20 and 21 show the best estimates for the velocity profiles from the topAWI platform. The differences between isolated up- (Figures 20a/21a) and downcast (Figures 20b/21b) are considerable. It is explained by the motion of the platform itself, which was not removed from the ADCP measurements. Figure 20 (a), for example, shows a very strong northward velocity at around 280 m depth. When the platform begins an upcast, going from the bottom to the surface, it will horizontally move away, i.e. southward from the northward-moving ship. Relative to the TRIAXUS, this motion will be measured as northward velocity. The velocity gradient is first very sharp and then gets smoother while going further up. The details of the movements are explained again below.

For comparison purposes, Figure 22 shows the velocity profiles from the vessel mounted ADCP (VMADCP) for the same transect. The white values at the bottom show gap, at the locations where

the measurements from the VMADCP were not accurate enough due to the large range. Plotted at the surface (0 - 10 m) is the velocity estimated from the ship-mounted wave radar *WaMoS*. The plotted value is a 20-minutes average over three rectangular surfaces of approximately 2 km^2 around the ship. The gaps in the radar data due to the lack of wind and waves were not large and therefore were filled using a simple nearest neighbour interpolation.
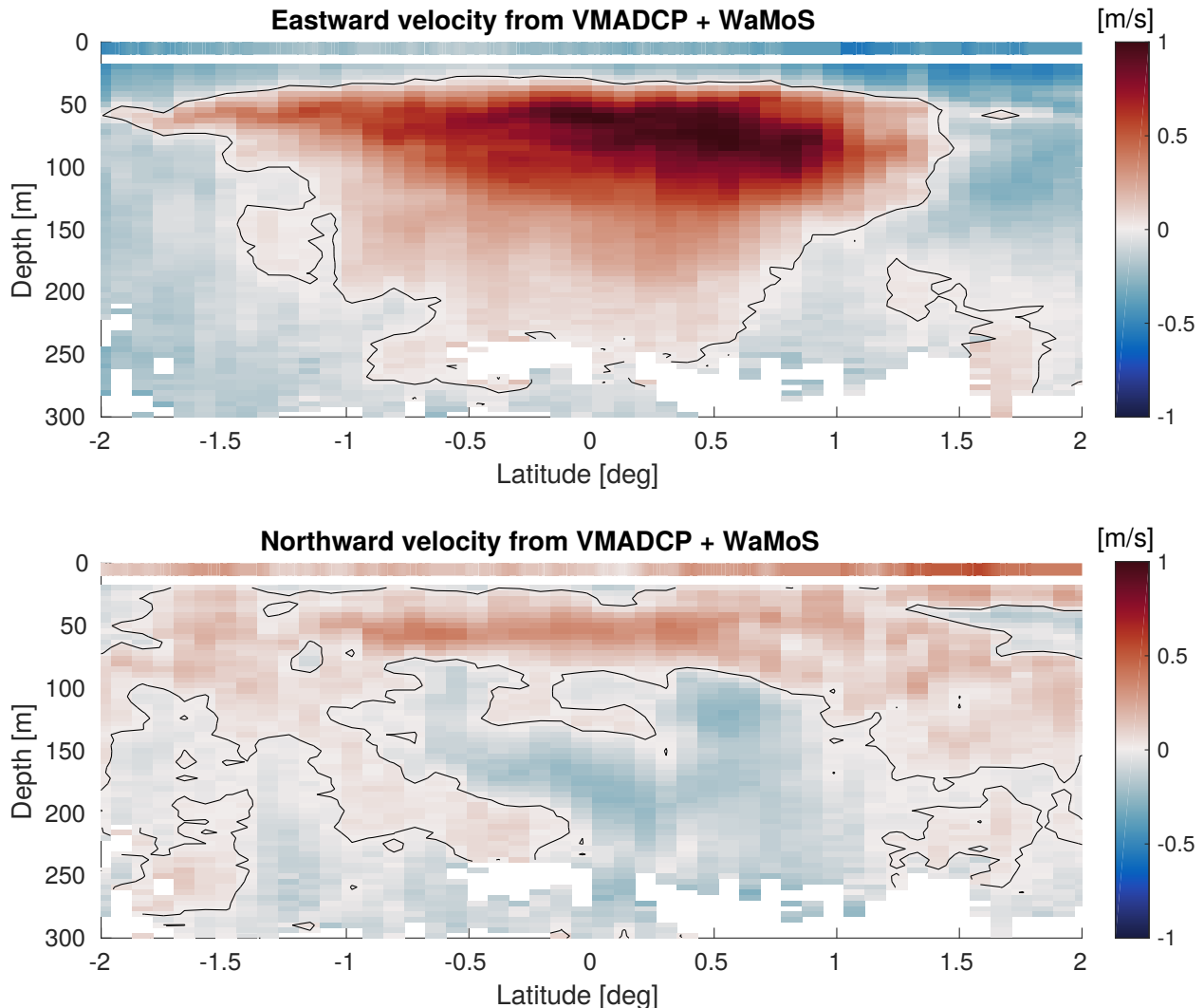

Figure 22: Velocity profiles from the vessel-mounted ADCP. In the top 10 m, the value for the surface current obtained with the sigma s6 WaMoS II Wave Radar system is plotted. The black contour line is the 0 velocity.

Figure 23 shows the difference between the VMADCP and topAWI velocity profiles. The difference between the up- and downcasts is again remarkable. First one can observe that the general position of the EUC is shallower as determined from the VMADCP (maximum velocities found at 60 m) than from the topAWI (maximum velocities at 80 m).

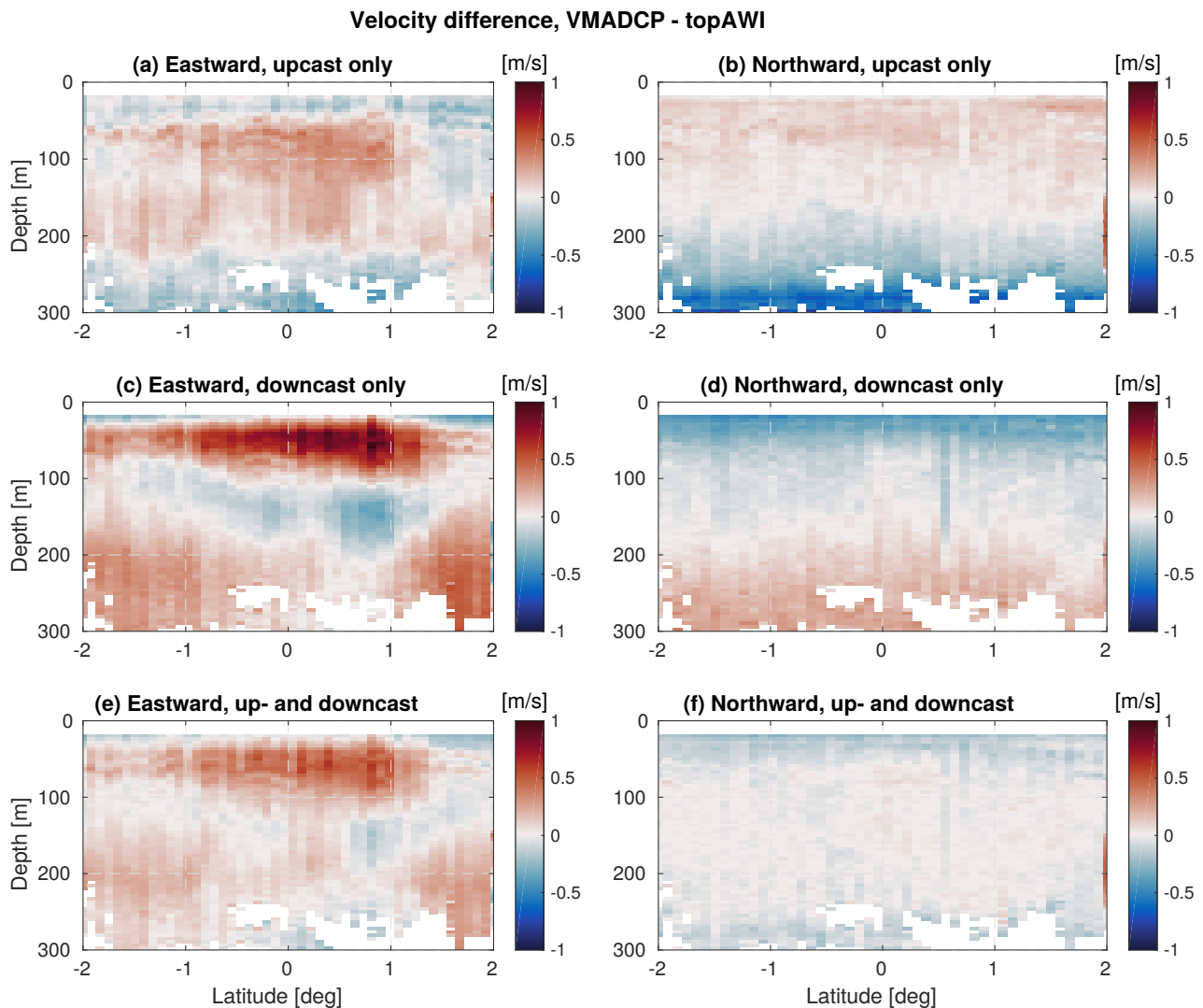**Velocity difference, VMADCP - topAWI**

Figure 23: Difference between velocity from VMADCP and topAWI. (a),(c),(e) are Figure 22a minus Figure 21a/b/c and (b),(d),(f) are Figure 22b minus Figure 20a/b/c. Positive values mean that the VMADCP measured velocities values were higher than the ones from topAWI.

Figure 23 permits a better assessment of the quality of the topAWI velocity profiles and to understand the TRIAXUS motions inside the water. First, one should keep in mind that the only active steering applied on the TRIAXUS on this dive concerned the depth, linked to the desired saw-tooth profile. Laterally, the platform was able to move as much as allowed by the length of the cable. Hence, when the TRIAXUS is crossing the EUC, it will get pushed along with the flow and the velocity at which it is moving will then have repercussions on the measured ones, by making them smaller than they are. Such an effect will be observed until the point where the platform reaches the maximum lateral extension. This point is called the cable neutral point and is found somewhere in the middle depth of the profiles, between 100 and 200 m depth. Then, the cable length is under the maximum tension and, therefore, can be further away from the ship. These lateral movements are symmetrically found as north- and southward velocities in the profiles (b) and (d). Indeed, while going up from 300 m depth in (b), the northward velocity is very high. The same happens for the downcast from the surface in (d). These velocities correspond to the movement to and back from the ship, as the cable oscillates around its neutral point. With the same logic the lateral movements of the platform can be seen in Figure 23 (a) and (c).

While for the case of the northward component, the up- and downcasts effects seems to annihilate well, such that mostly noise (f) remains, the same is not true for the eastward velocities in (e). The

eastward velocities observed at a depth of 50 m, followed by the westward ones at approximately 150 m depth in (e) mean that the EUC current from the topAWI is estimated deeper as the one from VMADCP.

Moreover, the ROTV vertical velocity is not always 1 m/s, as programmed. In reality, just before the turning point, the vehicle was slowing down a bit. This effect could also influence the measured velocity and was due to the flap controls for the trajectory.

Subsequently, the total transport from the equatorial undercurrent was estimated by the integration of all eastward velocity components over the occupied cross-sectional area. Whereas a value of 18.6 Sv was calculated based on the VMADCP profile, the topAWI profiles gave a total transport of 11.8 Sv. Based on the references found in the literature which were presented in Section 1.2, the value of 18.6 Sv seems more appropriate as an approximation for the middle of the Atlantic. Nonetheless, one has to keep in mind that the transport of the EUC may vary not only longitudinally but also seasonally and on shorter time-scales. A value of 11.8 Sv however, is significantly lower than the expected value of $\approx$20 Sv, according to Schott et al. (2003). Therefore, it appears that the VMADCP estimate is closer to reality. The smaller transport of the topAWI estimate is probably also influenced by the motions of the ROTV, as discussed with the velocity profiles in Figure 23.

Since it is extremely difficult to take into account vehicle motions without the knowing the exact position of the vehicle relative to the vessel, this is how far we have made the processing for the ocean velocity profiles.

4.2.3   TKE dissipation

Figure 24 presents the fits for ε for three representative locations of the studied transect – respectively the background deeper ocean, the EUC core and the shear layer above it. Note that one would assume the dissipation to be largest in the shear layer above the EUC and smallest in the background deeper ocean. The second and third order structure function methods are applied on respectively the left-hand and the right-hand side plots. Dark blue shows the data without the shear correction, which was used for the red fits, according to Equations 13 and 14. In cyan are the values corrected for the shear, which shows no improvement and no significant difference for the first r values on which the fit is applied. Because the x-axis is $r^{2/3}$ rather than r for the left-hand plots, the fits should be in both cases a straight line. Based on this requirement and the shape of D_2 estimates, the fit was chosen to be applied only on the first four values of r. Moreover, based on Equation 12, the values calculated for D_3 should always be negative, since both ε and r can only be positive values. This indicates an issue, happening at least in the case of Figure 24(d). In their paper, Horwitz and Hay (2017) state that a positive value of the D_3 estimate can result from a non-meaningful average, i.e. with not enough data averaged within a box for the velocity measurement. This likely also happens here.
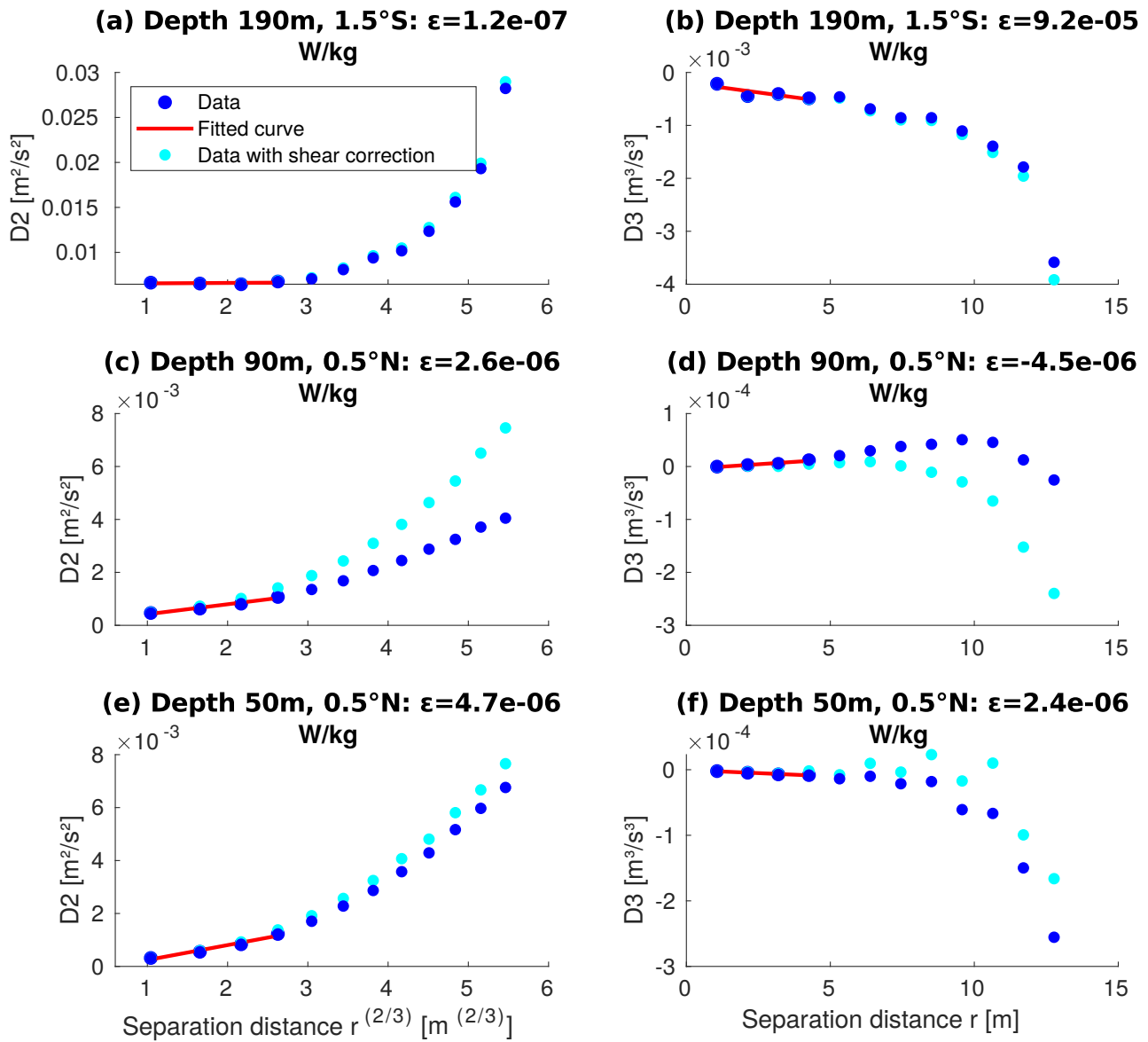
Figure 24: Second (a,c,e) and third (b,d,f) order structure function fits, for the background ocean (a),(b), inside of the EUC (c),(d) and just above the EUC (e),(f).

(a) Second order structure function: estimate for ε   [W/kg]

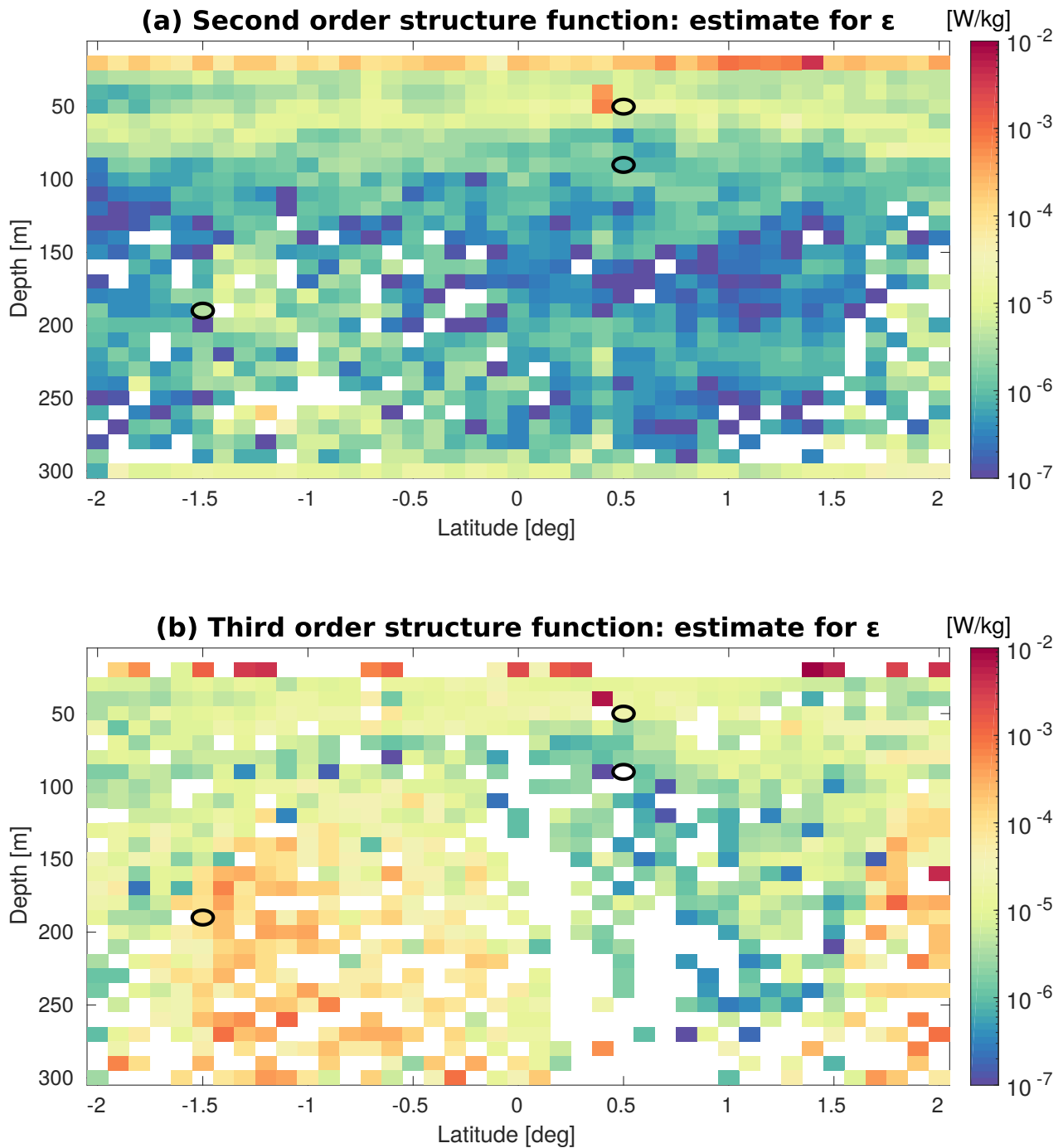**(b) Third order structure function: estimate for ε**   [W/kg]

Figure 25: Estimates for TKE dissipation in W/kg, for both the second order and third order structure function method. Straight line fits on the first four values of r were used. The color bar is in logarithmic scale. White values refer to ε estimates with an imaginary part in (a) and to estimates smaller or equal to 0 in (b). The black circles refer to the location of the three fits in Figure 24.

Figure 25 gives a spatial overview of the ε estimates which resulted from both the second order (a) and third order structure function method (b). Generally, the third order estimates tend to be larger than the second order ones. Also, the variance of the values from ε in Figure 25 (b) is bigger than the one from Figure 25 (a). It means that the values estimated from the third order structure function method are more spread around their mean. Lastly, one observes a pattern with increasing dissipation rate towards the surface, up to extreme values at 20 m depth. Two spots with large ε are also located on both sides of the EUC core between 150 and 300 m depth. The circles referring to the fits shown in Figure 25 indicates that, even if the second order structure function method works,

the third order can lead to negative, and thus absurd value (Figure 24d).

Hummels et al. (2013) show high ε values just above the EUC core, then decreasing going up to the surface until they rise again approaching the very first meters (Figure 3). At the EUC core position, they found values of 10^{-8} W/kg, which dropped to 10^{-9} W/kg under the current. In Figure 25, although higher values are observed closer to the surface, all the estimates appear to be a lot higher than what would be expected from the literature, i.e. by a factor of approximately 1000.

From a mathematical point of view, the third order structure function is an exact solution, i.e. with no requirement for an empirical constant. However, because it is to the power of 3, a small mistake in the velocity leads to a huge difference in the ε estimate. The fact that spatial patterns are found in Figure 25 suggests that the unlikely values may be the result of a systematic error. Instead, if it was only due to statistical errors, then Figure 25 would show random noise instead of patterns.

From this analysis, we conclude that smaller values of r might be needed to increase the quality of the linear fit. It is possible that only the first bin was under the Ozmidov scale in this particular case. A fit needs at least two good data points, but more to improve the accuracy. However, the bins have to be not too small either. Because the smallest resolved distances of the range offer more data points, there are more combinations between the bins can be averaged and lead to a better ε estimate. One would not want to lose these reliable estimates because they would be smaller than the Kolmogorov scale.

5 Summary and Discussion

5.1 Conclusions

The goal of this thesis was to assess the feasibility of using the topAWI platform for both velocity profiles and TKE dissipation rate estimation. For this purpose, the dataset of an Atlantic equatorial transect from the topAWI platform was used. The ROTV was undulating in a sawtooth profile from the surface down to 300 m depth. Two 1.2-MHz ADCP, respectively up- and downward looking were attached to the vehicle. Basic ADCP data processing steps were used to achieve velocity profiles. The absence of a working GAPS system made it impossible to exactly correct for the instrument motion. For the TKE dissipation, the second and third order structure functions were applied. There was a disagreement between the obtained results and the expected patterns. Therefore, the two most likely issues were raised. First, it could result from the use of the distance between bins values r, which are bigger than the Ozmidov scale. Since the structure function method only works within the inertial subrange, the results could be erroneous. Second, more individual raw data points for the estimation of ε could be needed to obtain a meaningful average.

On the EUC:

The observations at the equator turned out to be very helpful for the quality assessment of the data. The fact that the dynamics of the EUC are relatively well understood facilitates the assessment of the plausibility of the results, e.g. for transport and maximum velocity. In turn, the availability of the VMADCP velocity profiles enabled an in-depth comparison with the topAWI velocity profiles and a better understanding of the vehicle motions.

Important to keep in mind is that the profiles shown here were taken on one particular day. Due to its link to the global wind pattern, one would not expect major changes of the EUC within days. However, a significant difference may presumably be observed with varying month, according to the seasonal pattern of the ITCZ, as seen in Section 1.2. In the particular case of the EUC, due to its location at the equator, the dissipation varies with nighttime convection (Caldwell et al., 1997). In other parts of the ocean, hourly changes could be observed with e.g. tidal currents.

On the velocity profiles:

As the aim of this work was to assess the performance of the platform and not to get a deep understanding of the EUC, the velocity profile calculations were not carried on until their potentially final state. However, the actual setup of the topAWI seems well-adapted for profiling velocities. The major improvement that could be achieved would be to take into account the proper movements of the ROTV.

Also still missing is a robust and stand-alone routine for the quality assessment. As a matter of fact, some issues in the data were found by looking at the plots of the different variables together, e.g. with the CTD offset. As a result, such problems were corrected manually and have not been treated as general cases in the code. A complete routine would require a knowledge of all the possible issues and write a robust correction for all the encountered cases.

On the TKE dissipation rate estimation:

All in all, this transect permitted to bring to light the advantages and limitations of the structure function method. Even though being the exact solution, the third order structure function method is not found to be used extensively in the literature – only Horwitz and Hay (2017) used it. One of the reasons could be that, due to the error propagation the final error is bigger than with the second order structure function method. Moreover, for the latter, the values found in the literature for the constant C_v^2 hardly vary across papers and is therefore considered a reasonable estimate.

Given the ergodicity hypothesis, one could also use the VMADCP data as more estimates for the structure function method. However, in the present configuration, it would make only new data for r values of 4, 8 and 12 meters, being respectively 1, 2 and 3 times the bin differences of the VMADCP. This was not done in the scope of this project since the method was already giving questionable results and it appears that smaller values of r would be needed instead.

Another measurement source for the dissipation rate, e.g. with microstructure profilers, would give both a possibility to determine precisely the Ozmidov scale to know if the method is applicable, as well as a direct point of comparison in case the latter condition is fulfilled. However, it is clear that such measurements cost time and would stop the sawtooth profiles of the platform if taken from the same R/V. Some work has recently taken place to mount a shear probe directly onto an autonomous underwater vehicle (AUV). If this technology works, then a parallel transect of topAWI and this AUV could achieve good comparison with less ship time, even if the latter is slower. The main issue with the development of such a profiler is that shear probes are highly affected by any vibration, which is almost impossible to prevent on an AUV. Another solution to investigate would be the use of a high-frequency temperature sensor. Indeed, the variance of spectra of high-resolution temperature profiles, i.e. of a few cm, can be used for the determination of the overturning length.

On surface measurements:

In the scope of this work, the data from the upward-looking ADCP at the surface were removed, because they were showing extremely high values compared to what could be expected from the WaMoS radar data. For this reason, some data is lost at the surface. This fact could, however, be enhanced by the elaboration of a script, which would remove single-data points based on the echo intensity value which is highly dependent on the water surface. However, the ship wake has to be taken into account, which could affect the performance of ADCP measurements.

The existing literature on such effects is not broad, but for a first idea, Trevorrow et al. (1994) assessed the influence of microbubbles on acoustic measurements. Indeed, created by the ship motion, they act as scatterers and are observed within a width and depth of respectively approx. 65 m and 7-12.5 m. Moreover, they can still be detected up to 7.5 minutes after the vessel passed. The study was carried out on ships about half the size of R/V Polarstern. With a velocity of 10 knots, a persistence of 7 minutes would mean that the bubbles could be found near the surface up to approximately 2 kilometers behind the ship position.

5.2   Recommendations

In the final analysis, the present work reveals the importance of getting prior knowledge on the study area for the implementation of a structure function method to estimate ε from ADCP data. Undoubtedly, depending on both the Kolmogorov scale and the Ozmidov scale, the range of values in which the method applies can be very small. Furthermore, as the bin size and resolution is dependent on the hardware frequency of the ADCP, the latter should be chosen wisely and regarding the desired result.

The polar regions are the next to be explored with the help of the TRIAXUS. Therefore, to get an idea of what are the expected dissipation values in these parts of the ocean, one can refer to the literature. For example, the measurement campaign of Fer et al. (2016) in 2009 in the Weddell Sea, Antarctica, reveals values of ε ranging from 10^{-9}-10^{-8} W/kg for the first 100 m depth near the shelf break. Also in Antarctica, Thompson et al. (2007) determined turbulent dissipation values between 10^{-9}-10^{-7} W/kg from CTD casts. Between March and April 1989, measurements from Padman and Dillon (1991) on an ice camp revealed ε between 10^{-8}-10^{-6} W/kg for the region of Fram Strait. On the other side of the Arctic, at the Barrow Canyon, Shroyer (2012) found averaged ε between 10^{-9}-10^{-7} W/kg for different areas on a transect. All these estimates for TKE dissipation and their associated

Ozmidov scale are summarized hereafter in Table 3. For most of the estimates, the Ozmidov scale was calculated using Equation 5 with the values taken from the figures in the papers. However, the range of values determined using the color bars of the plots was often uncertain, and a small change in the ε value can lead to a very different Ozmidov scale. Hence, the values have to be taken as rough indications.

Table 3: Estimates of TKE dissipation, buoyancy frequency and Ozmidov scale for diverse locations, based on literature.

Location	Expected ε [W/kg]	N [1/s]	Ozmidov scale [m]	Source
Weddell Sea	$10^{-9} - 10^{-8}$	$10^{-3} - 10^{-2}$	0.0004-0.002	Fer et al. (2016)
Drake Passage	$10^{-9} - 10^{-7}$	$10^{-3} - 10^{-2}$	0.08-4	Thompson et al. (2007)
Fram Strait	$10^{-8} - 10^{-6}$	$10^{-2.5} - 10^{-2}$	0.1-3	Padman and Dillon (1991)
Barrow Canyon	$10^{-9} - 10^{-7}$	$10^{-2.5} - 10^{-1.5}$	0.006 - 5	Shroyer (2012)
Equatorial Atlantic	$10^{-7} - 10^{-6}$	$10^{-5} - 10^{-3.5}$	0.1 - 5	Hummels et al. (2013)

The papers of Whalen et al. (2012) and Waterhouse et al. (2014) also give an overall idea of ε values for various locations in the oceans. Figure 26 shows the estimates from the paper of Whalen et al. (2012). As expected, the abyssal ocean shows very small values. For the average dissipation rate between 250 and 500 m depth, one can observe that usually, the values are higher near the coasts, especially in the western boundary currents of the Pacific, Indian and Atlantic oceans. Globally, the values for the Southern Ocean seem quite low, except for the Drake Passage (between Cape Horn and Antarctica) and an area south of the Tasman Sea between New Zealand and Australia.
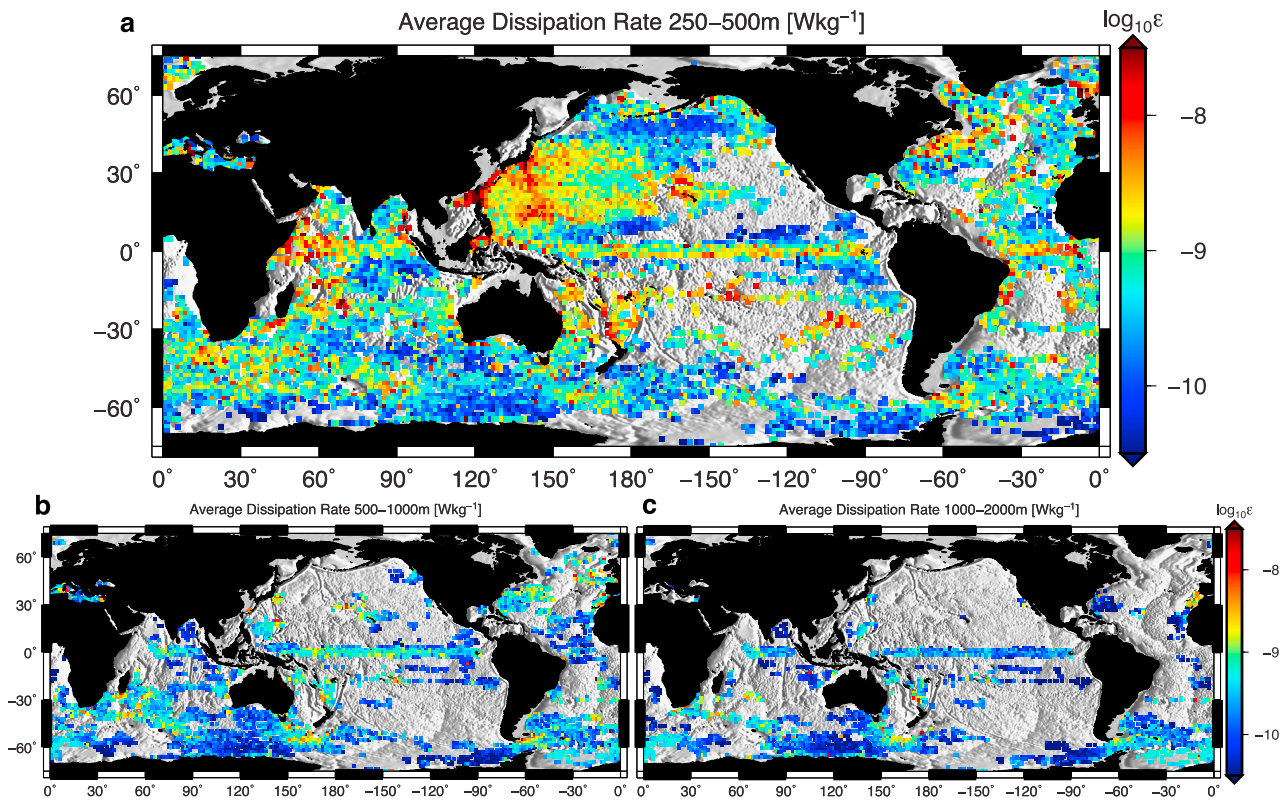
Figure 26: TKE dissipation [W/kg] from Argo float profiles for a 1.5° grid and three different depth ranges (Whalen et al., 2012). Estimates consist of at least 3 estimations of ε derived from buoyancy measurements from Argo following the method of Kunze et al. (2006).

Since the Ozmidov scale gives the size of the largest overturning eddies, and since the structure function method only applies within the inertial subrange, i.e. smaller than the Ozmidov scale, one wants to make sure to be able to resolve such a scale. Hence, the values of the Ozmidov scale in Table 3 can be used to formulate recommendations on diverse areas for the bin size. As also seen in the results, a high number of estimates is necessary to reduce the error sufficiently. The number of estimates depends on the frequency of the ADCP. The bin size itself, in turn, is also dependent on the frequency of the ADCP – a higher frequency allowing for a smaller bin size to be resolved.

As a rule of thumb, the largest distance between the bins should be able to resolve the biggest Ozmidov scale. So that in the case of a rather turbulent location such as the Equatorial Atlantic or the Barrow Canyon, the bin size should ideally be of the order of 10 cm. Whereas in the open ocean as in the Weddell Sea, the bin size should be less than a millimeter, which is not possible.

Once the desired bin size and frequency are defined, the hardware and software requirements can be calculated with, e.g. the software tool PlanADCP by Teledyne RDI which can be downloaded from *http://www.teledynemarine.com/rdi/support* upon registering.

As achieving a millimeter-scale bin size requires a higher frequency ADCP than currently available on the market, the method seems currently not suitable for low turbulence regions. Greene et al. (2015) found a way to reduce the sensor noise using the large-eddy method, which requires another setup, where a beam of the ADCP needs to be vertical, but this can also be an avenue for further instrument/method development.

However, one also has to keep in mind that using high-frequency ADCP and small bins will, in turn, impact the quality of the velocity profiles that can be achieved with the same configuration. Because of the reduced range, the coverage of the ADCP may then not be able to estimate the velocities over the entire transect, depending on the platform trajectory and velocity. Of course, to

be able to get the best velocity profiles, one would then ideally use another lower frequency ADCP only for the velocity profiles. But in the case of the TRIAXUS, this is not always possible. Indeed, the number of instruments that can be mounted on it is restricted by the optical cable connections, the power requirement and by the total size and weight that has to be compensated with buoyancy foam. Therefore, the design of the ADCPs on topAWI directly depends on the desired purpose of the measurements. For some very turbulent regions, one can maybe achieve the two purposes together, for other less turbulent regions two pieces of hardware may be needed.

Finally, regarding the velocity profiles only, having the GAPS working on the TRIAXUS would simplify the processing steps a lot. Knowing the exact position of the platform relative to the vessel would avoid approximations, i.e. for the cable length, and lead to much better quality velocity profiles.

6 Acknowledgments

Bibliography

Blanke, B., M. Arhan, A. Lazar, and G. Prévost, 2002: A Lagrangian numerical investigation of the origins and fates of the salinity maximum water in the Atlantic. *Journal of Geophysical Research: Oceans*, **107 (C10)**, 27–1.

Blanke, B., and S. Raynaud, 1997: Kinematics of the Pacific equatorial undercurrent: An Eulerian and Lagrangian approach from GCM results. *Journal of Physical Oceanography*, **27 (6)**, 1038–1053.

Boyd, J. P., 2018: *Dynamics of the Equatorial Ocean.* Springer.

Butt, J., and E. Lindstrom, 1994: Currents off the east coast of New Ireland, Papua New Guinea, and their relevance to regional undercurrents in the western equatorial Pacific Ocean. *Journal of Geophysical Research: Oceans*, **99 (C6)**, 12 503–12 514.

Caldwell, D., R.-C. Lien, J. N. Moum, and M. C. Gregg, 1997: Turbulence decay and restratification in the equatorial ocean surface layer following nighttime convection. *Journal of Physical Oceanography*, **27 (6)**, 1120–1132.

Claret, M., R. Rodríguez, and J. L. Pelegrí, 2012: Salinity intrusion and convective mixing in the Atlantic Equatorial Undercurrent. *Scientia Marina*, **76 (S1)**, 117–129.

Crawford, W. R., and T. R. Osborn, 1980: Microstructure measurements in the Atlantic Equatorial Undercurrent during GATE. *Oceanography and Surface Layer Meteorology in the B/C Scale*, Elsevier, 285–308.

Dietrich, G., K. Kalle, W. Krauss, and G. Siedler, 1975: *Allgemeine Meereskunde: Eine Einführung in die Ozeanographie.* Gebr. Borntraeger.

Fer, I., E. Darelius, and K. B. Daae, 2016: Observations of energetic turbulence on the Weddell Sea continental slope. *Geophysical Research Letters*, **43 (2)**, 760–766.

Gargett, A. E., 1999: Velcro measurement of turbulence kinetic energy dissipation rate ε. *Journal of Atmospheric and Oceanic Technology*, **16 (12)**, 1973–1993.

Góes, M., and I. Wainer, 2003: Equatorial currents transport changes for extreme warm and cold events in the Atlantic Ocean. *Geophysical Research Letters*, **30 (5)**, 8006, doi:10.1029/2002GL015707.

Greene, A., P. Hendricks, and M. Gregg, 2015: Using an ADCP to estimate turbulent kinetic energy dissipation rate in sheltered coastal waters. *Journal of Atmospheric and Oceanic Technology*, **32 (2)**, 318–333.

Henry, D., 2018: Nonlinear Features of Equatorial Ocean Flows. *Oceanography*, **31 (3)**, 22–27.

Horwitz, R. M., and A. E. Hay, 2017: Turbulence dissipation rates from horizontal velocity profiles at mid-depth in fast tidal flows. *Renewable Energy*, **114**, 283–296.

Hummels, R., M. Dengler, and B. Bourlès, 2013: Seasonal and regional variability of upper ocean diapycnal heat flux in the Atlantic cold tongue. *Progress in Oceanography*, **111**, 52–74.

Knauss, J. A., 1960: Measurements of the Cromwell current. *Deep Sea Research*, **6**, 265–286.

Kolmogorov, A. N., 1941: Dissipation of energy in locally isotropic turbulence. *Dokl. Akad. Nauk SSSR*, Vol. 32, 16–18.

Kunze, E., E. Firing, J. M. Hummon, T. K. Chereskin, and A. M. Thurnherr, 2006: Global abyssal mixing inferred from lowered ADCP shear and CTD strain profiles. *Journal of Physical Oceanography*, **36 (8)**, 1553–1576.

Lilly, J. M., 2017: jLab: A data analysis package for Matlab, v. 1.6.5. http://www.jmlilly.net/jmlsoft. html.

Lucas, N., J. Simpson, T. Rippeth, and C. Old, 2014: Measuring turbulent dissipation using a tethered ADCP. *Journal of Atmospheric and Oceanic Technology*, **31 (8)**, 1826–1837.

MacArtney Underwater Technology, 2019: TRIAXUS - Oceanographic ROTV system. 2nd edition - 2.1. Accessed: 2019-01-17, https://www.macartney.com/media/6445/triaxus.pdf.

NOAA Office of Ocean Exploration and Research, 2018: Operational SST Anomaly Charts for 2018. Accessed: 2019-03-20, https://www.ospo.noaa.gov/Products/ocean/sst/anomaly/2018.html.

Ozmidov, R. V., 1965: Certain features of the energy spectrum of oceanic turbulence. **161 (4)**, 828–831.

Padman, L., and T. M. Dillon, 1991: Turbulent mixing near the Yermak Plateau during the coordinated Eastern Arctic Experiment. *Journal of Geophysical Research: Oceans*, **96 (C3)**, 4769–4782.

Pan, J., and D. A. Jay, 2008: A method for processing acoustic Doppler current profiler velocity data from towed, undulating vehicles. *Journal of Atmospheric and Oceanic Technology*, **25 (9)**, 1710–1716.

Peters, H., M. Gregg, and J. Toole, 1988: On the parameterization of equatorial turbulence. *Journal of Geophysical Research: Oceans*, **93 (C2)**, 1199–1218.

RD Instruments, 1989: Acoustic Doppler Current Profilers. Principles of operation: a practical primer. *RD Instruments, San Diego*.

Schott, F. A., and Coauthors, 2003: The zonal currents and transports at 35 W in the tropical Atlantic. *Geophysical Research Letters*, **30 (7)**, 1349, doi:10.1029/2002GL016849.

Shroyer, E. L., 2012: Turbulent kinetic energy dissipation in Barrow Canyon. *Journal of Physical Oceanography*, **42 (6)**, 1012–1021.

Stramma, L., M. Rhein, P. Brandt, M. Dengler, C. Böning, and M. Walter, 2005: Upper ocean circulation in the western tropical Atlantic in boreal fall 2000. *Deep Sea Research Part I: Oceanographic Research Papers*, **52 (2)**, 221–240.

Strass, V., 2018a: Links to master tracks in different resolutions of POLARSTERN cruise PS113 (ANT-XXXIII/4), Punta Arenas - Bremerhaven, 2018-05-08 - 2018-06-11. doi:10.1594/PANGAEA.891753, URL https://doi.org/10.1594/PANGAEA.891753.

Strass, V., 2018b: The Expedition PS113 of the Research Vessel POLARSTERN to the Atlantic Ocean in 2018. *Berichte zur Polar-und Meeresforschung= Reports on polar and marine research*, **724**, doi:10.2312/BzPM_0724_2018, URL https://doi.org/10.2312/BzPM_0724_2018.

Talley, L. D., G. L. Pickard, W. J. Emery, and J. H. Swift, 2011: Chapter 9 - Atlantic Ocean. *Descriptive Physical Oceanography (Sixth Edition)*, L. D. Talley, G. L. Pickard, W. J. Emery, and J. H. Swift, Eds., Sixth Edition ed., Academic Press, Boston, 245 – 301, doi:https://doi.org/10.1016/B978-0-7506-4552-2.10009-5, URL http://www.sciencedirect.com/science/article/pii/B9780750645522100095.

Thébault, E., and Coauthors, 2015: International geomagnetic reference field: the 12th generation. *Earth, Planets and Space*, **67 (1)**, 79.

Thompson, A. F., S. T. Gille, J. A. MacKinnon, and J. Sprintall, 2007: Spatial and temporal patterns of small-scale mixing in Drake Passage. *Journal of Physical Oceanography*, **37 (3)**, 572–592.

Thorpe, S. A., 2005: *The turbulent ocean.* Cambridge University Press.

Trevorrow, M. V., S. Vagle, and D. M. Farmer, 1994: Acoustical measurements of microbubbles within ship wakes. *The Journal of the Acoustical Society of America*, **95 (4)**, 1922–1930.

Voituriez, B., and A. Herbland, 1979: The use of the salinity maximum of the Equatorial Undercurrent for estimating nutrient enrichment and primary production in the Gulf of Guinea. *Deep Sea Research Part A. Oceanographic Research Papers*, **26 (1)**, 77–83.

Waterhouse, A. F., and Coauthors, 2014: Global patterns of diapycnal mixing from measurements of the turbulent dissipation rate. *Journal of Physical Oceanography*, **44 (7)**, 1854–1872.

Whalen, C., L. Talley, and J. MacKinnon, 2012: Spatial and temporal variability of global ocean mixing inferred from Argo profiles. *Geophysical Research Letters*, **39 (18)**, L18 612, doi:10.1029/2012GL053196.

Wiles, P. J., T. P. Rippeth, J. H. Simpson, and P. J. Hendricks, 2006: A novel technique for measuring the rate of turbulent dissipation in the marine environment. *Geophysical Research Letters*, **33 (21)**, L21 608, doi:10.1029/2006GL027050.
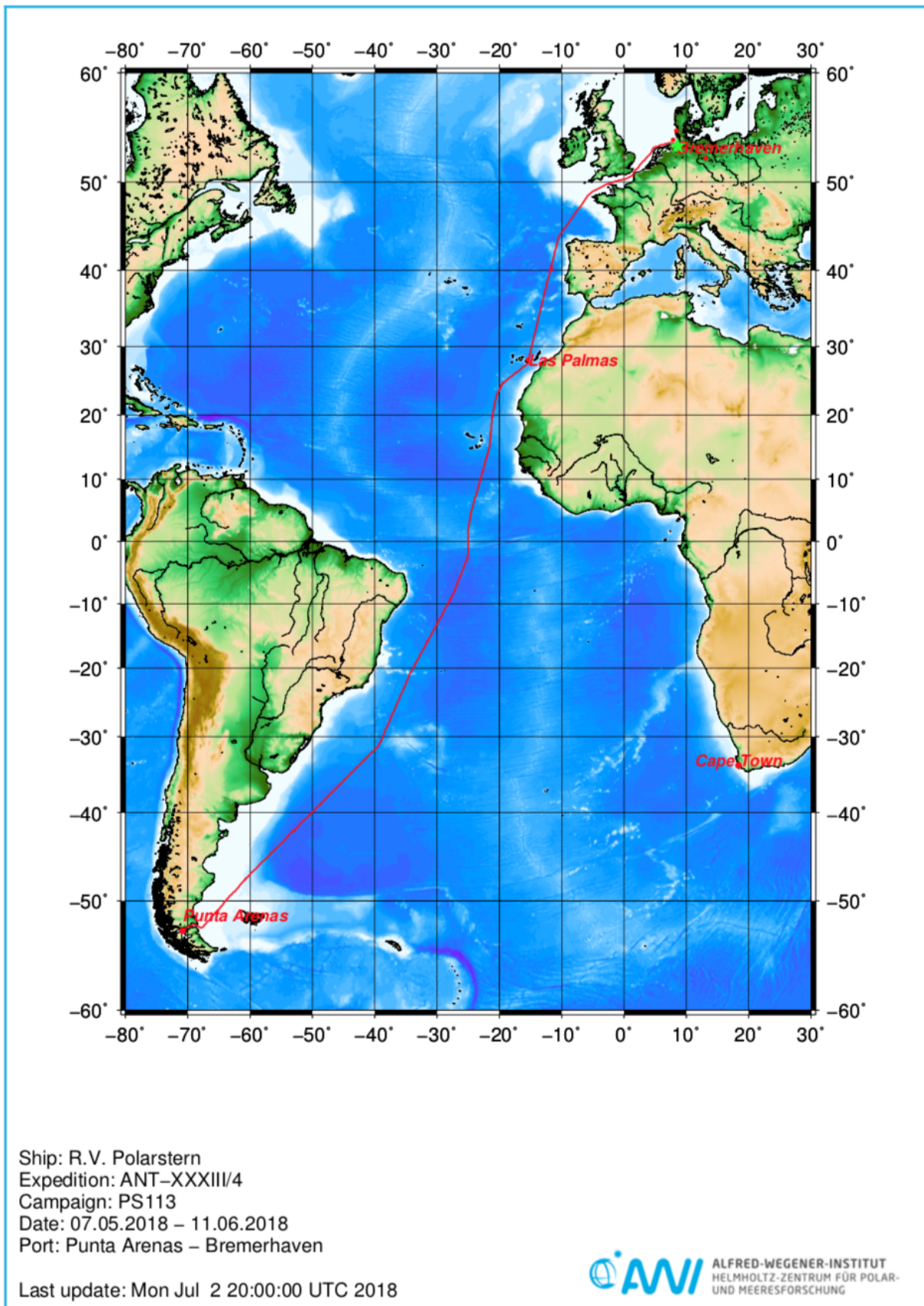
Appendix

Ship: R.V. Polarstern
Expedition: ANT–XXXIII/4
Campaign: PS113
Date: 07.05.2018 – 11.06.2018
Port: Punta Arenas – Bremerhaven

Last update: Mon Jul 2 20:00:00 UTC 2018

ALFRED-WEGENER-INSTITUT
HELMHOLTZ-ZENTRUM FÜR POLAR-
UND MEERESFORSCHUNG

Figure A1: Overall path of R/V Polarstern during the cruise PS113. The master track can also be found following this link: *https://doi.pangaea.de/10.1594/PANGAEA.891753* (Strass, 2018a)
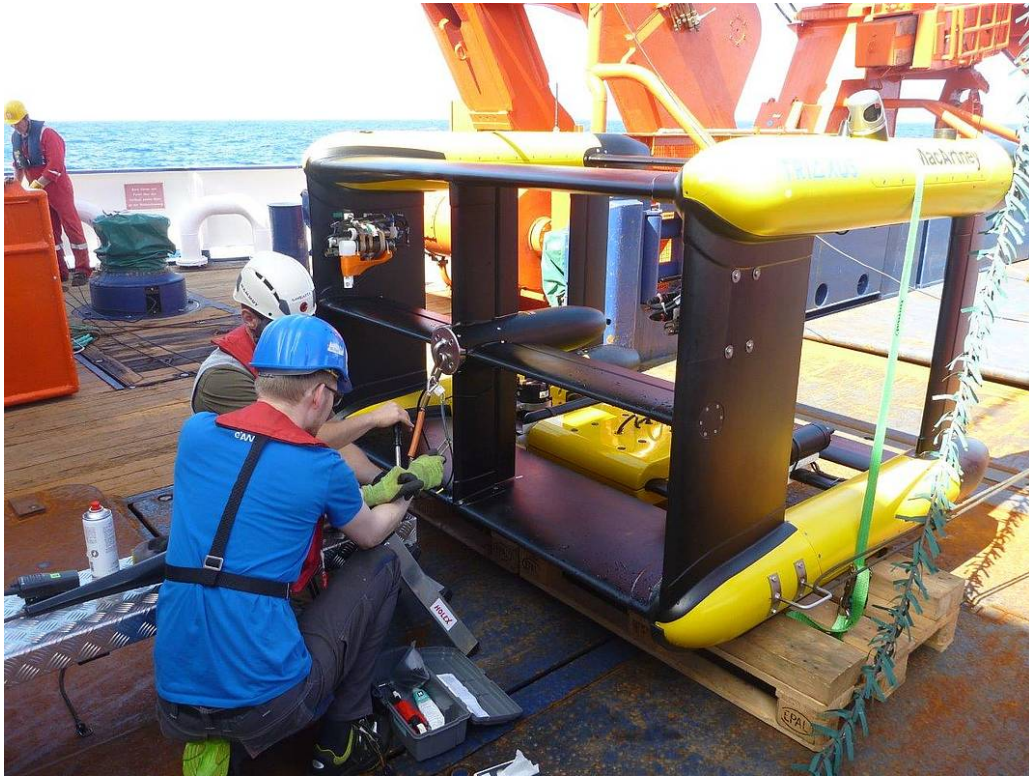
Figure A2: Plugging the optic fiber connection before the dive. Picture: Volker Strass, AWI
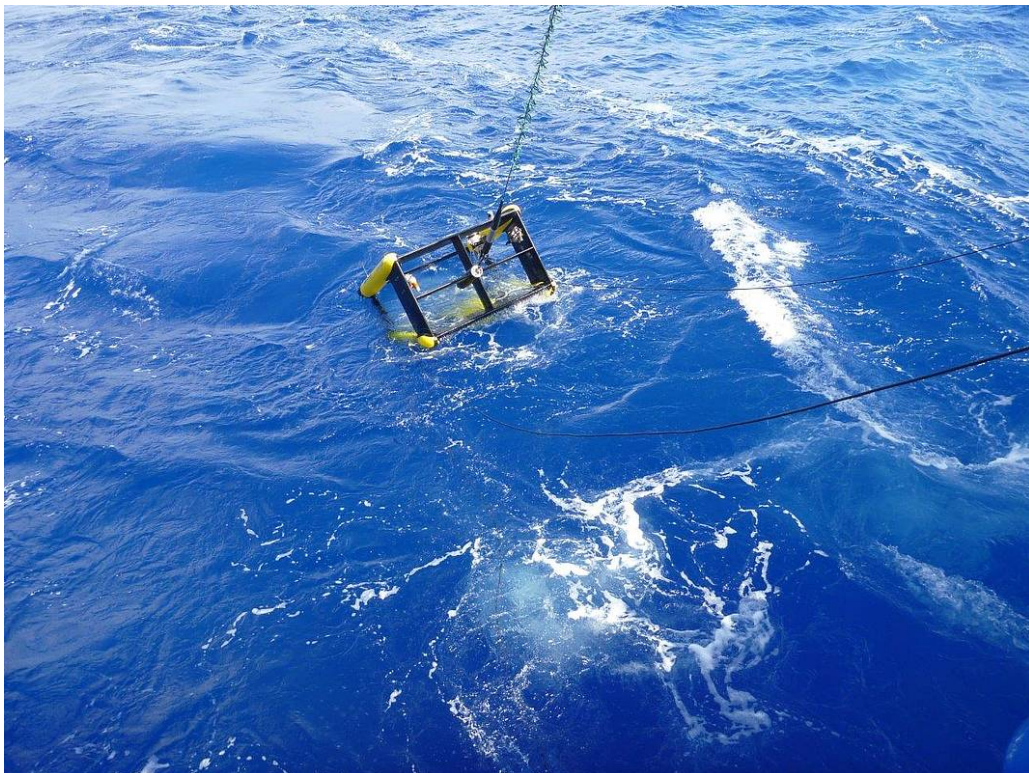

Figure A3: One of the technical difficulties: lowering the TRIAXUS into the water. Picture: Volker Strass, AWI